A multi-hazard analysis framework for earthquake-damaged tall buildings subject to thunderstorm downbursts

Song, Jing; Skalomenos, Konstantinos; Martinez-Vazquez, Pedro

DOI:
10.1002/eqe.3825

Received: 1 July 2022 | Revised: 4 January 2023 | Accepted: 8 January 2023

DOI: 10.1002/eqe.3825

WILEY

RESEARCH ARTICLE

A multi-hazard analysis framework for earthquake-damaged tall buildings subject to thunderstorm downbursts

Jing Song | **Konstantinos Skalomenos** | **Pedro Martinez-Vazquez**

Department of Civil Engineering, University of Birmingham, Edgbaston, Birmingham, UK

Correspondence
Konstantinos Skalomenos, Department of Civil Engineering, University of Birmingham, Edgbaston, Birmingham B15 2TT, UK.
Email: k.skalomenos@bham.ac.uk

Abstract

This study develops a generalised multi-hazard analysis framework for evaluating the impact of secondary hazard events on structures that have previously been damaged by major hazardous events. More specifically, the present work investigates the effects of thunderstorm downbursts on earthquake-damaged tall steel buildings giving an emphasis in assessing the revised accumulated earthquake-wind ductility demands. The novel approach is validated on a 20-storey steel building. The structure is initially subjected to a ductility-controlled pushover analysis to simulate the earthquake-induced damage, and then, a parametric dynamic analysis is performed using damaged structure models under synthetic downburst time-histories developed for various wind profiles, wind velocities and terrain types. The method accurately controls the damage level induced by the primary hazard and separately assesses secondary hazard effects which enables a direct quantification of the new multi-hazard design requirements. This can provide effective guidance in the stage of preliminary structural design or post-hazard assessment of structures identifying new serviceability limits, as well as support repair procedures and decision-making frameworks for existing structures to prevent collapse. The results demonstrate a significant increase up to three to four times in ductility demands of the structure after the occurrence of the strong downburst winds, compared with the ductility demands that were initially imposed by the varying severity degrees of the earthquake.

KEYWORDS

earthquake-wind finite element analysis, multi-hazard ductility demands, restart analysis, tall steel buildings, thunderstorm downburst

NOVELTY

- A novel multi-hazard analysis framework for assessing structural performance to sequential lifetime hazardeous events is proposed.
- The adaptive pushover analysis is combined with the dynamic time history analysis through a novel restart analysis algorithm for simulating multi-hazard effects.
- The effect of thunderstorm downbursts on earthquake-damaged tall steel buildings is investigated for a first time giving an emphasis in assessing the revised accumulated earthquake-wind ductility demands.
- This study can provide effective guidance in identifying new serviceability limits under multi-hazards, as well as support repair procedures and decision-making frameworks for existing structures.

1 | INTRODUCTION

Factual evidence shows that structures that have been damaged during previous primary hazard events are prone to secondary damage induced by subsequent hazards, such as, aftershocks, tsunamis, hurricanes, tornadoes, thunderstorms.[1,2] This may increase post-disaster damage of structures that remained exposed after the primary event, which severely undermines the serviceability of the structure. On the other hand, very strong secondary subsequent events could even cause collapse of the damaged structures. Slender steel structures are vulnerable to damaging vibrations, such as earthquakes and microbursts, and current design guidelines ignore these multi-hazard effects that are likely to occur within the lifespan of a structure as separate events.

The increased frequency of severe thunderstorms observed over recent decades like downbursts has motivated researchers to study this complex natural phenomenon.[3,4] Thunderstorm downbursts are distinguished from synoptic winds as transient non-stationary winds. The strong downdraft flow from thunderstorms accelerates downwards, and when it reaches the ground, it can produce divergent intense outflows, as shown in Figure 1. Vortices induced by the wind shear are formed during this process, accompanying the generation of the significant sharp increase in the wind velocity. This phenomenon can cause damage equivalent to synoptic wind flow of 75 m/s within a time interval range of 5–20 min.[5,6] Due to the 'nose shape' profile at varying heights above the ground, the height of the maximum wind speed of outflow is located between 30 and 100 m above the ground level,[7] which is obviously different with synoptic winds. Most recently, the dynamic responses of structures under thunderstorm downbursts have been investigated by a variety of methods, including: (a) the stochastic theoretical model developed by Caracoglia,[8] (b) the response spectral technique proposed by Solari and De Gaetano,[9] (c) the generalised wind loading chain developed by Kareem et al.,[10] (d) the non-stationary

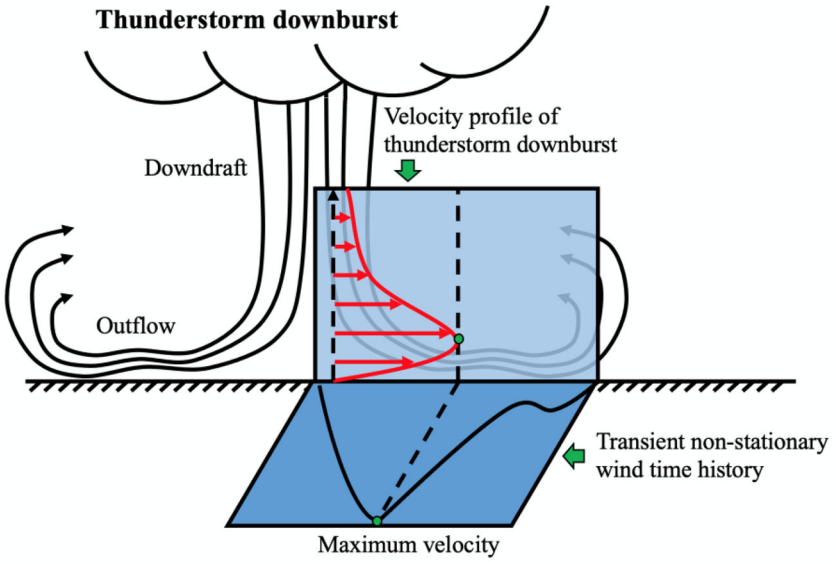

FIGURE 1 Velocity profile of thunderstorm downburst.

probabilistic model developed by Ciano et al.,[11] and (e) the thunderstorm downburst design spectrum introduced by Song et al.[12]

Previous researchers have highlighted the risk associated with the collapse mechanism of tall structures under earthquakes or thunderstorm downbursts.[13–15] The state of the art still identifies important knowledge gaps spanning from the design aspects to the development of contingency plans and strategies to increase structural resilience. The current design guidance[16–18] evidences such limitations, as it disregards the occurrence of multiple hazard events, such as earthquakes and strong winds, within the design life of a structure. The risk of exceeding the limit states can be twice in regions with significant wind and seismic hazard events compared with the regions governed by a single hazard, while the seismic performance of buildings designed to primary withstand wind loads can be very poor even under low-amplitude events.[19–23]

To understand the impact of wind and earthquake vibrations on structural performance, recent researchers have utilised probability-based techniques for multi-hazard structural analysis. Martinez-Vazquez[24] and Martinez-Vazquez et al.[25] stressed the necessity of consideration for the combined effect of earthquakes and strong winds, since this may drive the structures into their inelastic response obviously increasing ductility demands. Martin et al.[26] proposed fragility surfaces for multi-hazard analysis and assessment of suspension bridges under earthquakes and microbursts. Roy et al.[27] developed a multi-hazard framework for investigating high-rise base-isolated buildings under sequential multiple earthquakes and winds likely to occur in the design life of a structure. Kwag et al.[28] transferred a probabilistic risk-assessment framework into a deterministic performance-based framework to consider multiple hazards in structural design, and other studies have focused on the development of vibration control systems for tall buildings to reduce multi-hazard vibrations.[29,30]

Most of the studies above have mainly focused either on generating multi-hazard scenarios or assessing structural performance under multiple hazards by applying each hazard separately, thus ignoring possible subsequent effects (e.g. damage accumulation, fatigue, strength and stiffness deterioration). There are a few studies that account for sequential multi-hazard effects,[1,2,27] but their proposed analysis frameworks require the execution of all hazard analysis in series which is time-consuming and may induce uncertainties by the selection of each event. A more direct analysis framework that builds upon the existing well-established knowledge of single-hazard analysis without requesting its repetition would allow for a more rapid transition from the single-hazard design to multi-hazard design reflecting the current knowledge. This approach can be possible if the secondary hazard analysis can be applied directly to structural models that include already the response information and damage induced by the major single-hazard event.

Based on the above methodological approach, this paper aims to develop a generalised multi-hazard analysis framework for evaluating the impact of secondary hazard events on structures that have experienced previously a demanding major hazardous event. This will allow the direct quantification of the additional design requirements as dictated by the secondary hazard event alone. The present work investigates for a first time the effects of thunderstorm downbursts on earthquake-damaged tall steel buildings giving an emphasis in assessing the revised accumulated earthquake-wind ductility demands. The proposed methodology combines the general principles of the nonlinear adaptive pushover analysis,[31,32] which aims to reproduce the damages induced by the major earthquake event, with the subsequent dynamic time-history analysis, which aims to estimate the damages induced by the secondary hazard event, the thunderstorm downburst. The proposed multi-hazard analysis algorithm offers a robust implementation of seismic pushover analysis and wind time-history analysis within a restart analysis framework that allows a parametric study to be performed focusing on the impact of the secondary hazard event by investigating various downburst wind profiles, wind velocities and terrain types. The method accurately controls the damage level induced by the major event, thus eliminates uncertainties, and separately assesses secondary hazard effects which enables a direct quantification of the additional design requirements. This can provide effective guidance in the stage of structural design under multi-hazards or post-hazard assessment of new structures, as well as support repair procedures and decision-making frameworks for existing structures.

The present study consists of six sections in addition to Introduction (Section 1). Section 2 outlines the concept and methodology of the multi-hazard analysis framework. Section 3 describes the design of a 20-storey steel building frame modelled in ABAQUS[33] and its validation through pushover seismic analysis results. Section 4 presents the generation of 11 synthetic thunderstorm downburst wind fields for the examined structure considering varying heights of maximum slowly varying mean velocity (30, 50 and 70 m), varying vertical profiles of turbulence intensities (Terrain types 0, I, II, III, IV from Eurocode[17]) and varying maximum velocities (30, 50 and 70 m/s). Section 5 presents the dynamic response of the frame model subject to downburst wind loads alone. Section 6 presents the multi-hazard analysis results under earthquake loads and thunderstorm downbursts. The paper ends with Section 7, which summarises the main findings of this study.

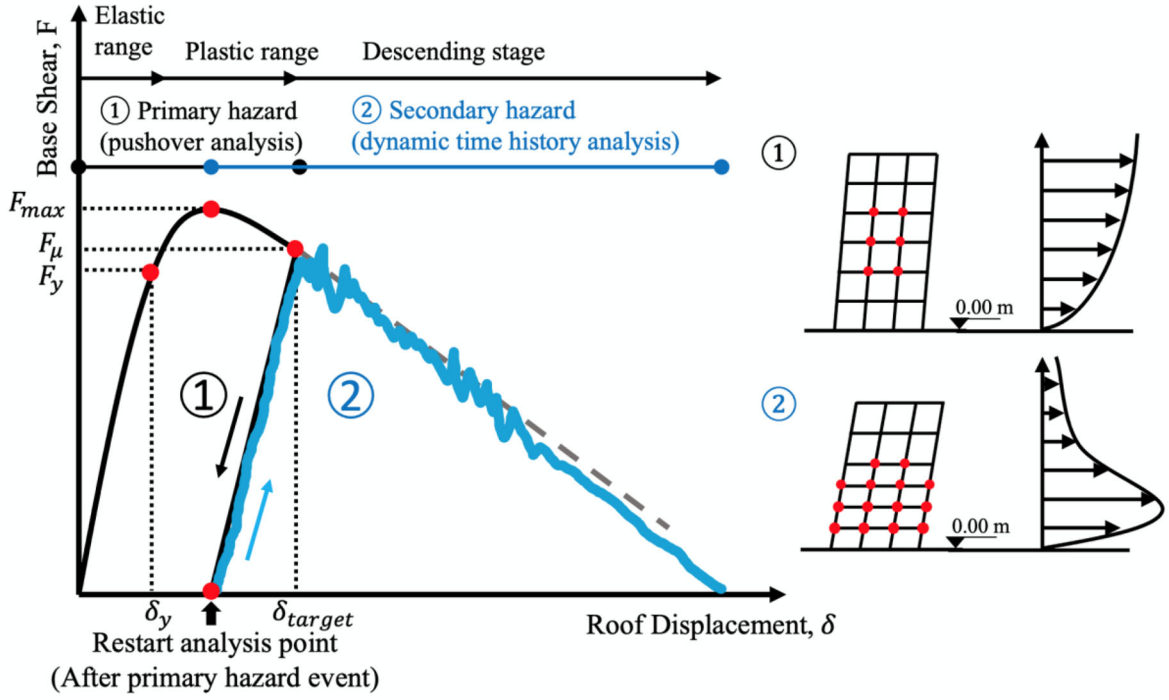

FIGURE 2 Diagram of the proposed multi-hazard analysis procedure.

2 | MULTI-HAZARD ANALYSIS FRAMEWORK

Figure 2 schematically illustrates the overall concept of the proposed multi-hazard analysis framework. The computational procedure combines two classical analysis methods which are performed in two phases: (a) the pushover nonlinear analysis which is executed first to drive the structure into a target deformation state (assumed to be induced by the primary hazard), followed by (b) a set of dynamic time history analysis, which is performed within a restart analysis framework that allows for repetition and random reloading of the previously deformed structure. This sequential analysis is further described by the following four steps:

***Step 1*: Apply axial loads**.

Gravity and live loads are calculated and applied in the structure model using a general static analysis method of ABAQUS.[33] Appropriate modelling is considered to account for the second-order effects induced by storey drifts and mass.

***Step 2*: Perform frequency analysis for obtaining the initial lateral load pattern**.

This step calculates the modal shapes of the structure, which are used to obtain the lateral load pattern following the lateral force distribution method by Chopra and Goel.[34] Higher vibration modes can be combined for the determination of the lateral load pattern.

***Step 3*: Adaptive controlled pushover analysis for the primary hazard event (see ① in Figure 2)**.

This step links ABAQUS[33] pushover capabilities to MATLAB[35] optimization procedures to perform an adaptive controlled pushover analysis following the method recommended by Skalomenos and Papazafeiropoulos.[36] This approach uses a novel mixed force/displacement optimization control algorithm to trace the plastic range of the structural response. The Step 2 is repeated through a restart analysis framework, which is executed during the pushover analysis in order to update the lateral load pattern (force distribution is continuously updated according to the calculated eigenmodes of the structure and the progress of the global plastic deformation mechanism). The adopted control algorithm can: 1) lead to a more realistic global deformation of the structure and determination of the overall plastic mechanism to collapse than the conventional pushover analysis due to the adaptive force control, and 2) induce to the structure specific ductility demands by taking the advantage of the mixed force/displacement restart control which allows the user to settle the structure to zero-force equilibrium after the end of the pushover analysis, as shown in Figure 2 (unloading to permanent plastic deformations). Notwithstanding, ABAQUS[33] has its own stabilisation algorithms or arc-length control (Riks) methods, these

do not suffice for an adaptive pushover analysis. Static analysis with Riks can trace only a single loading path during the analysis and does not allow the user to control the force distribution pattern during the analysis.[35] Moreover, it does not distinguish between loading-unloading directions, which opens the possibility that the analysis may unload the structure from the last converged equilibrium point with the load vector pointing in the wrong direction. For this reason, a restart pushover analysis with general static process controlled by MATLAB[35] is set in this study to ensure that the structure reached zero-force equilibrium when the original pushover terminates.

Furthermore, the pushover analysis enables a direct quantification of the structural capacity creating one frame model that contains all nonlinearities and stress state of the earthquake-damaged structure, which can be 're-loaded', as it is for the subsequent secondary hazard analysis. It is obvious that the generation of a similar earthquake-damaged frame model cannot be achieved by executing a set of time-history analysis since each earthquake motion leads to a different damage state, thus different earthquake-damaged models. The use of pushover analysis to envelop the capacity of the damaged structure and control the earthquake-induced ductility demands appears to be simpler and more direct method for the purpose of this study. Following the proposed framework, one can also execute cyclic pushover analysis[37] to account for the cyclic behaviour of members under fully controlled conditions. Figure 2 (labelled with ①) schematically illustrates a typical base shear-roof displacement relationship as obtained during the pushover analysis. The roof displacement can be controlled to reach a pre-defined ductility level caused by the primary hazard event.

***Step 4*: Transient non-stationary wind analysis of the secondary hazard event (see ② in Figure 2).**

A subsequent hazard analysis can be performed by reading the output file of the previously deformed structure and further loading the structure. This is done with ABAQUS[33] libraries that enable the user to stop the analysis at a desired time point and restart at the same or another time point before.[38,39] As a result, a subsequent hazard analysis can be performed by reading the output file of the previously deformed structure and subjecting the same structure to any type of new. In the present study, the subsequent analysis simulates a secondary hazard taking place after the structure has reached a pre-defined ductility level during the primary hazard. The restart microburst simulation uses a force control mechanism based on the direct-integration implicit dynamic algorithm available in ABAQUS.[33] The dynamic time history analysis follows the pushover analysis after settling the structure to zero-force equilibrium (permanent plastic deformations), see label ② in Figure 2.

The subsequent dynamic analysis is transient fidelity. There the Hilber-Hughes-Taylor integrators are $\alpha = -0.05$, $\beta = 0.27$, and $\gamma = 0.55$.[40] The maximum increment size had to be consistent with the time step of the recorded wind load time history, that is, 0.3068 s - see Section 4. The initial increment size to help convergence is 0.01. All the restart analytical steps are consistent with the results of the previous phase as the setting FREQUENCY in the input files equals 1 when calling the restart analysis.

3 | PUSHOVER ANALYSIS OF A TALL STEEL STRUCTURE

3.1 | Building prototype

For this investigation, a 20-storey building designed according to the Uniform Building Code[41] was created in ABAQUS (2020). The model consists of beam-column elements and has a total height of 78.68 m including the basement, as shown in Figure 3. The ground and the first floor have a 4.57 m height while all other floors separate by 3.66 m. The dimensions of the plan view are 36.6 m × 24.4 m with a 6.1 m bay width in either direction. The terrain type corresponds to exposure B with a basic wind speed of 31 m/s. The earthquake resisting design corresponds to Zone 4 (soil type S2), where the base shear coefficient is 0.03 and the drift limitation is 0.025. Gravity loads acting on floors and roof equal 6.23 and 3.59 kPa, respectively, which complements with a cladding load of 1.44 kPa.

The building is subjected to lateral loads acting in the weak direction of the building. Considering the symmetry of this building, one exterior moment resisting frame (MRF) and one interior equivalent gravity frame (GF) are used to represent half of the building; columns in the interior GF are integrated through generalised sectional properties. The sectional area and the moment of inertia in major and minor directions for the columns are scaled to represent 2½ gravity frames whereas local mass lumps at building joints.

The two frames connect at each storey level through pinned Link elements and multi-point constraints (MPC) to approximate diaphragmatic rigidity. Steel is assumed elastic isotropic with modulus of elasticity E = 210 GPa, yield and ultimate

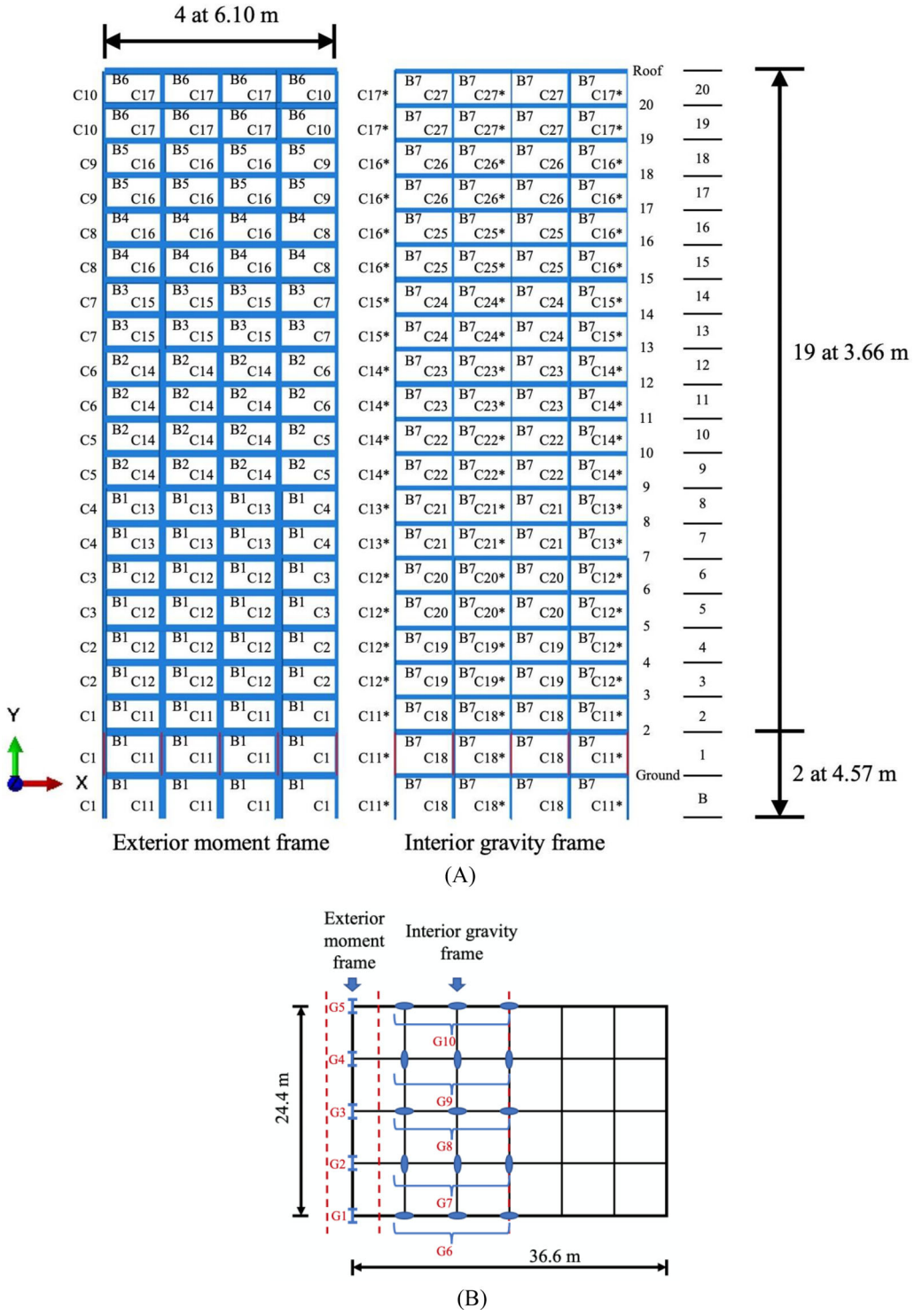

FIGURE 3 Basic information of frames for the 20-storey steel building, * represents weak axis orientation,[42] (A) 2-D model view; (B) Plan view of the entire building.

stress of 248 and 400 MPa, respectively, and Poisson ratio $\nu = 0.3$. The specific weight $\rho = 7850$ kg/m^3 yields a half weight of the building of 54.46 MN.

The bottom of the basement columns of the building frame are fully constrained since lateral restraints added to the ground floor. The beam connections in the exterior moment frame are fully fixed while the beam connections in the interior GF are pinned. Table 1 lists the characteristics of columns and beams.

TABLE 1 The dimensions for the column and beam elements of 20-storey building frame in Figure 3.[42]

Label	Element	Label	Element	Label	Element
C1	W14×370	C13	W30×173	C25	W14×74
C2	W14×342	C14	W27×178	C26	W14×61
C3	W14×311	C15	W24×162	C27	W14×53
C4	W14×283	C16	W24×146	B1	W30×124
C5	W14×257	C17	W21×122	B2	W30×116
C6	W14×211	C18	W14×176	B3	W30×108
C7	W14×176	C19	W14×159	B4	W30×99
C8	W14×159	C20	W14×145	B5	W27×94
C9	W14×132	C21	W14×120	B6	W27×84
C10	W14×109	C22	W14×109	B7	W21×50
C11	W30×211	C23	W14×99		
C12	W30×191	C24	W14×90		

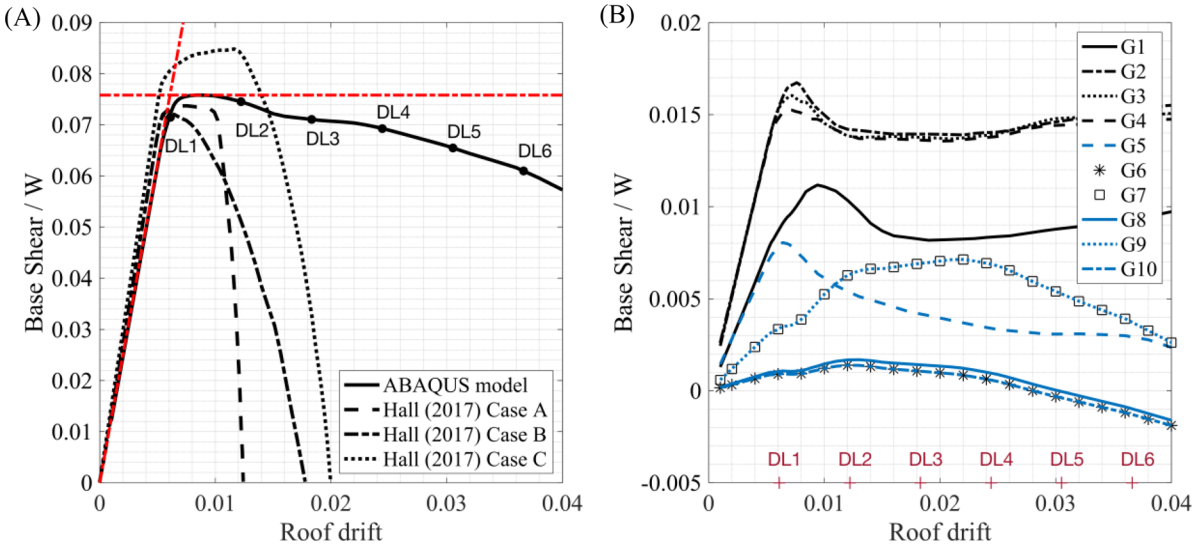

FIGURE 4 Pushover curves (base shear force at the ground level is normalised by the frame weight; roof drift represents the roof displacement divided by the overall height of the building), (A) entire frame model; (B) each column.

3.2 | Validation of the building model

The fundamental period of the building is 4.01 s, which turns out to be higher than the 3.63 s reported by Hall.[42] This is attributed to the pinned connections specified at the ends of beams across the GF. Noting that Hall's model[42] reduced the strength and stiffness of beams in 10% to simulate pinned connections, hence approximations are implicit in both models.

Figure 4A compares the pushover curves as obtained from ABAQUS, with three case studies examined by Hall.[42] Those cases correspond to separate modelling approaches: (a) Case A ignores strength and stiffness of the GF while accounting for hardening and softening of steel with plastic hinges; (b) Case B disregards hardening and softening; and (c) Case C fully integrates all factors. The new model built in ABAQUS considers perfect pins for the GF beams while the stain hardening effect is accounted to the inelastic beam-column material performance of the rest of the members using a bi-linear stress-strain relationship for steel. These assumptions are close to those made for the Case A[42] with the difference that softening response of steel members is not simulated in the present study. Figure 4A shows that the initial stiffness and peak strength are consistent with Hall's case studies,[42] especially with Case A, where the difference is 2% for the yielding strength, 3% for the ultimate strength and 9% for the elastic stiffness. The extended branch of the curve drops less steeply in the ABAQUS model due to the absence of hinge softening, thus bringing the point of the gravitational instability at higher roof drift.

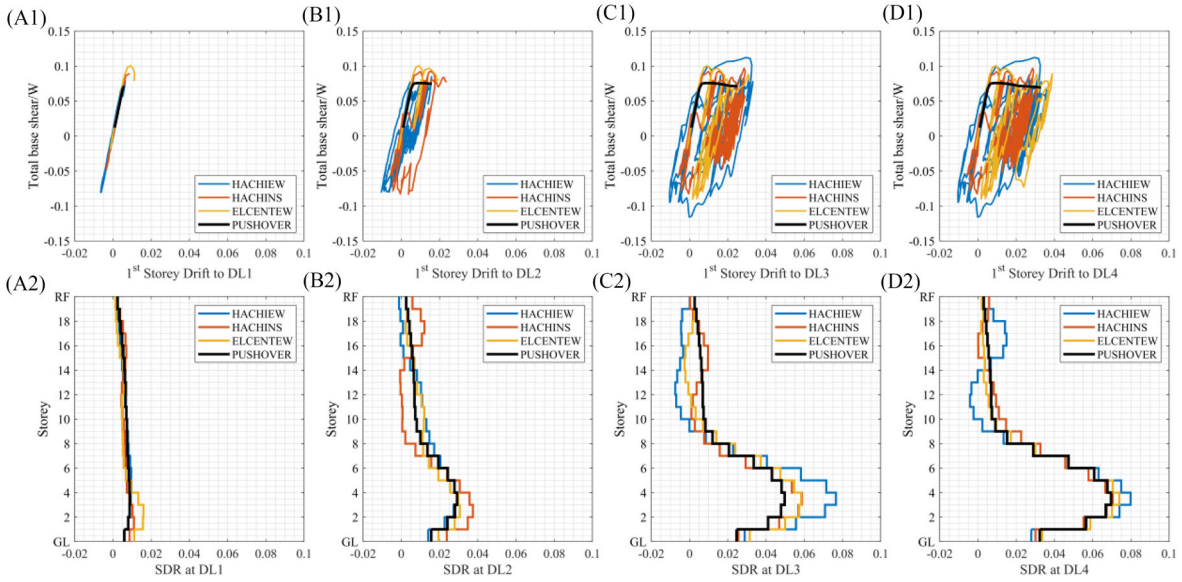

FIGURE 5 Comparison of the results between pushover analysis and dynamic time history analysis.

This enables a validation of the proposed multi-hazard algorithm in a wide range of ductility demands avoiding sudden strength drops that could have resulted in the termination of analysis.

In Figure 4A, the yield point at the intersection of the red dashed lines is identified, following Castiglioni et al.[43] The intersection is defined by the projected gradient of elastic stiffness and the maximum base shear.

In this study, Equation (1) is used to calculate the target ductility, which in the following paragraphs is also referred to as DL, for example, μ_1 is equivalent to DL1 (see Figure 4A).

$$\mu_i = \frac{\delta_{target}}{\delta_y} \tag{1}$$

In Equation (1), δ_{target} is the target roof drift and δ_y is the yielding drift. Accordingly, δ_{target}= 0.0061, 0.0122, 0.0183, 0.0244, 0.0305 and 0.0366, for the sequence DL-N where $1 \leq N \leq 6$ is estimated. The yielding drift is therefore $\delta_y = 0.0061$.

Figure 4B reports the ratio between base shear (normalised with the total weight (W) of the structure) and roof drift, for each column at the ground level. G1-G10 labels columns located at the extreme of the 2D frame, as identified in Figure 3. In Figure 4, a rapid strength decrease is observed on columns G6, G8 and G10 after reaching DL4, which is attributed to the position of the frame within the complex, which imposes higher loads that at the extremes, as well as to the orientation of the columns with respect to the direction of the loads applied, which exposes their weak axis. In addition, the higher moment of inertia of columns G2, G3 and G4 than columns G1 and G5 results in higher shear strength for the former columns. The variation in shear strength between G1 and G5 is due to the higher axial loads imposed to G5 due to the overturning moment (moment-axial interaction effect).

3.3 | Earthquake-induced damage by the pushover analysis

This section compares the pushover analysis results with those obtained by dynamic nonlinear time history analyses (NTHA). Three recorded earthquake motions (i.e. Hachinohe-EW, Hachinohe-NS and El Centro-EW) are chosen for the NTHA in this study. The ground motions are scaled in order to drive the structure to the ductility levels of DL1, DL2, DL3 and DL4, respectively. For each ductility level, the relationship between the base shear and the first storey drift are plotted in Figure 5(A1)–(D1) against the corresponding pushover analysis results. In addition, Figure 5(A2)–(D2) compare the storey drift ratios (SDRs[1]) profile from the NTHA with the SDR profile as obtained from the pushover analysis under the same ductility levels. This comparison demonstrates the consistency of the proposed pushover analysis to provide a reasonable estimation of the overall plastic deformation mechanism of tall building structures that cover all the way from elastic behaviour to final global dynamic instability and collapse. A more extensive validation of the

proposed pushover analysis and powerfulness of its adaptive algorithm for more case studies is a subject of a future study.

4 | SIMULATION OF THE THUNDERSTORM DOWNBURST WIND FIELD

The hybrid theoretical procedure by Chen and Letchford[44] for simulating an artificial downburst wind velocity field was adopted for this investigation. The method comprises three key steps: (1) generation of a random signal to represent wind velocity time series using the approach suggested by Priestley,[45] subject to reduced turbulent fluctuations as proposed by Deodatis[46] while using the power spectral model proposed by Solari et al.[47] – see Equation (2); (2) calibrating wind time series to fit the slowly varying mean velocity that reproduces the profile of horizontal wind proposed by Wood et al.,[48] which incorporates the time function suggested by Holmes and Oliver[49]; and (3) integration of the downburst velocity field, as explained by Chen and Letchford,[44] this is $U(z,t) = \bar{U}(z,t) + u'(z,t) = \bar{U}(z,t) + \sigma_u(z,t)\tilde{u}'(z,t) = \bar{U}(z,t) + I_u(z)\bar{U}(z,t)\tilde{u}'(z,t)$. In this equation, z is the height above the ground, t is the time, $\bar{U}$ is the slowly varying mean velocity, u' is the fluctuating wind velocity, σ_u is the slowly varying standard deviation (dealt with as a modulation function), $\tilde{u}'$ is the reduced turbulent fluctuation taken as a rapidly varying stationary Gaussian random field and I_u is the turbulence intensity.

$$\frac{nS_{\tilde{u}'}(z,n)}{\sigma_u^2(z)} = \frac{18\left(\frac{nz}{\bar{U}_{max}(z)}\right)}{\left[1+27\left(\frac{\omega z}{2\pi\bar{U}_{max}(z)}\right)\right]^{5/3}} \tag{2}$$

In Equation (2), n is the frequency of gust wind, ω is the circular frequency and $\bar{U}_{max}$ is the maximum slowly varying mean velocity.

Due to the limited evidence on the effective variation of thunderstorm downburst induced turbulence with height, the turbulence intensity is approximated with that representing synoptic winds while following recommendations by ASCE7.[16] The cut-off circular frequency is assumed to be 4 rad/s, and the number of circular frequency steps (N) equals 2048. It was considered reasonable to set the sampling frequency of the simulated fluctuation to 2.56 Hz. Furthermore, the reference velocity and reference height correspond to the peak value (36.5 m/s) of the slowly varying mean velocity at 13 m height for a 50-year return period, as recommended by Solari et al.[47] and Solari et al.[50] This procedure enabled generating 20 velocity time series for various wind events covering the height range 4.75–74.11 m, spaced by 3.66 m to align time series with the frame storey heights. This method preserves key characteristics of the downburst winds such as the exact location of the maximum horizontal velocity, the correct discretisation of the slowly varying mean velocity, and the target turbulence intensity profile, which are further described in the following paragraphs.

4.1 | Varying height of $\bar{U}_{max}$

The 3-s peak velocity time histories at the height of maximum slowly varying mean velocity, $\bar{U}_{max}$, that is, $z_{\bar{U}_{max}} = 30$, 50 and 70 m above the ground, are demonstrated in Figure 6A. The maximum velocities for the study U_{max} stand as of 59, 63 and 68 m/s for $z_{\bar{U}_{max}} = 30$, 50 and 70 m, respectively. This defines three different velocity profiles along the building height, thus affecting the lateral input load distribution and energy absorption capacity of the building. The terrain category is exposure B. The vertical velocity profiles of the peak horizontal wind are illustrated in Figure 6B where the dashed lines depict smoothed trendlines.

4.2 | Varying vertical profiles of I_u

Figure 6C provides variations of peak velocity with the building height, that correspond to terrain types 0, I, II, III and IV as per Eurocode.[17] This figure confirms that the increase of soil roughness induces higher peak velocities along the height, noting that the slowly varying mean velocities and the rapidly varying turbulent fluctuations are consistent with the wind

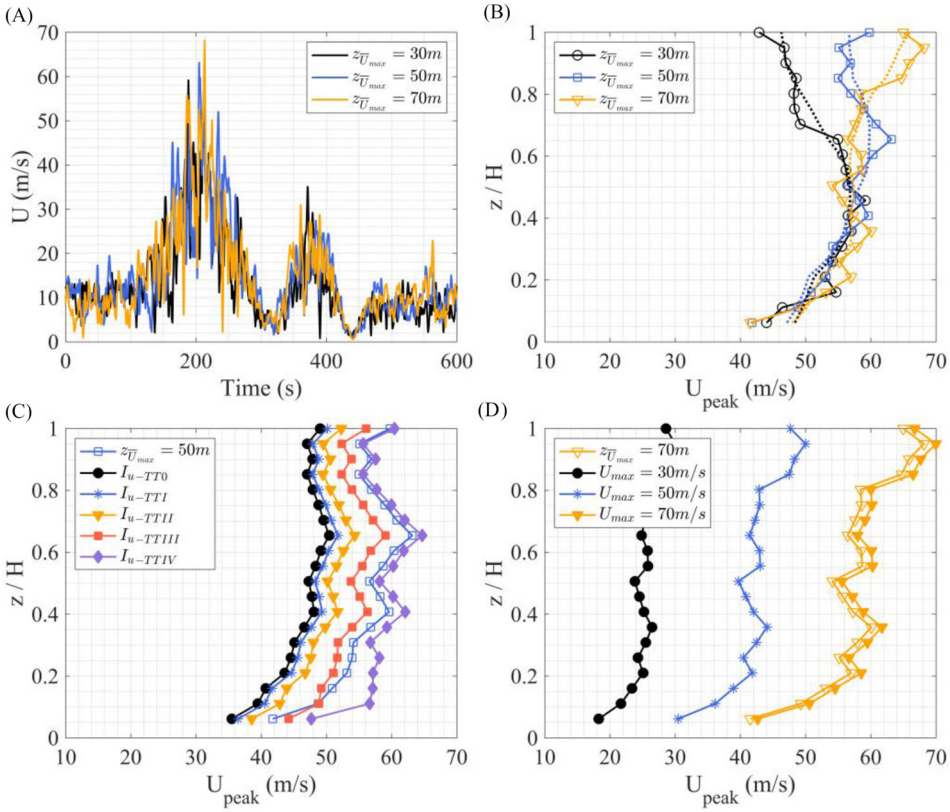

FIGURE 6 Horizontal and vertical profiles of downburst velocity, (A) Horizontal velocity time history at the height of maximum velocity; (B) Peak velocity at each storey with varying $z_{\bar{U}_{max}}$; (C) Peak velocity at each storey with varying vertical profiles of I_u; (D) Peak velocity at each storey with varying U_{max}.

field shown in Figure 6A where $z_{\bar{U}_{max}}$ was fixed to 50 m above the ground. The turbulence intensity profiles above the ground under different terrain types naturally lead to variable slowly varying standard deviations of the simulated velocity time histories. In these five profiles, the resulting maximum velocities are 50, 52, 54, 59 and 65 m/s.

4.3 | Varying U_{max}

The downburst wind field shown in Figure 6A, that is, $z_{\bar{U}_{max}}$ = 70 m, has been normalised by the maximum velocity to 30, 50 and 70 m/s, respectively, and the vertical profiles of the peak velocities are shown in Figure 6D. The downburst wind loads are then calculated by $f(z,t) = C_d \times 0.5\rho U(z,t)^2 A$ where A represents the storey area exposed to wind. The drag coefficient C_d is assumed equal to 1.2[51] and the air density ρ is taken as 1.225 kg/m^3. The terrain category for the simulation corresponds to exposure B whereas the pressure coefficient used for calculating wind loading was assumed independent of height, due to the lack of experimental evidence that better describes spatial variations of this parameter.

5 | THUNDERSTORM DOWNBURST WIND ANALYSIS

This section presents analysis results under the synthetic wind profiles alone. These results are used as reference data for comparison with data obtained from the multi-hazard analysis in a later section. The 11 synthetic downburst wind profiles listed in Table 2 were applied to the undamaged building to determine the base shear-roof drift relationship for each synthetic load shown in Figure 7. It can be observed from this figure that the deformations of the building are within the elastic range under downburst wind profiles 1, 3, 4, 5, 9 and 10, all corresponding to ductility demands below 1, that is, 0.91, 0.95, 0.81, 0.88, 0.19 and 0.51, respectively, see Table 2. In contrast, some plastic performance occurs when the structure

TABLE 2 Summarised ductility demand[a](maximum roof drift[b]) for eleven downburst wind profiles (Profile 1–3 for varying $z_{\bar{U}_{max}}$; Profile 4–8 for varying I_u; Profile 9–11 for varying U_{max})

Wind profile	$Z_{\bar{U}_{max}}$ (m)	I_u	U_{max} (m/s)	Wind load	DL1	DL2	DL3	DL4	DL5	DL6
	Step-by-step static pushover				1.00 (0.0061)	2.00 (0.0122)	3.00 (0.0182)	4.00 (0.0244)	5.00 (0.0305)	6.00 (0.0366)
P1	30	B	59	0.91 (0.0056)	1.00 (0.0061)	2.00 (0.0122)	2.98 (0.0182)	3.98 (0.0243)	5.08 (0.0310)	11.74 (0.0716)
P2	50		63	1.57 (0.0096)	1.62 (0.0099)	3.05 (0.0187)	11.52 (0.0703)	12.07 (0.0736)	11.37 (0.0694)	11.67 (0.0712)
P3	70		68	0.95 (0.0058)	1.01 (0.0062)	2.17 (0.0132)	3.34 (0.0204)	4.60 (0.0281)	12.61 (0.0769)	11.71 (0.0714)
P4	50	TT0	50	0.81 (0.0049)	1.00 (0.0061)	2.00 (0.0122)	3.07 (0.0187)	4.23 (0.0258)	5.36 (0.0327)	7.18 (0.0438)
P5		TTI	52	0.88 (0.0054)	1.00 (0.0061)	2.02 (0.0123)	3.14 (0.0192)	4.30 (0.0262)	11.84 (0.0722)	11.96 (0.0730)
P6		TTII	54	1.03 (0.0063)	1.08 (0.0066)	2.16 (0.0132)	3.30 (0.0201)	4.47 (0.0273)	12.45 (0.0759)	11.60 (0.0708)
P7		TTIII	59	1.33 (0.0081)	1.38 (0.0084)	2.47 (0.0151)	3.73 (0.0228)	12.58 (0.0767)	12.28 (0.0749)	11.26 (0.0687)
P8		TTIV	65	1.9 (0.0116)	1.93 (0.0118)	3.67 (0.0224)	13.03 (0.0795)	11.60 (0.0708)	11.12 (0.0678)	12.56 (0.0766)
P9	70	B	30	0.19 (0.0011)	1.00 (0.0061)	2.00 (0.0122)	2.98 (0.0182)	4.00 (0.0244)	5.00 (0.0305)	6.00 (0.0366)
P10			50	0.51 (0.0031)	1.00 (0.0061)	2.00 (0.0122)	2.98 (0.0182)	4.00 (0.0244)	5.10 (0.0311)	6.23 (0.0380)
P11			70	1.02 (0.0062)	1.06 (0.0065)	2.23 (0.0136)	3.42 (0.0209)	5.34 (0.0326)	13.11 (0.0800)	11.74 (0.0716)

[a]Ductility demand denotes the maximum non-linear roof displacement divided by the yielding roof displacement of the overall structure.
[b]Maximum roof drift denotes the maximum roof displacement divided by the total height of the building.

is subject to wind profiles 2, 7 and 8, where the corresponding ductility demands equal 1.57, 1.33 and 1.9, respectively, which also relate to peak non-linear displacement of 0.75, 0.64 and 0.91 m (see Figure 8B), respectively. The main reason for this can evidently be associated to the larger maximum velocities recorded in the wind profiles, that is, 63, 59 and 65 m/s, respectively, but in particular to the vertical coordinate that holds $\bar{U}_{max}$ – that is 50 m. This load configuration thus imparts higher energy amounts than others in which the position of $\bar{U}_{max}$ moves to either the top or base of the building. Furthermore, Figure 8A and 8B plot the profile of the maximum SDRs and maximum displacements along the building height, respectively. One can observe larger SDRs at the bottom half of the building under the downburst wind profiles 2, 7 and 8.

Figure 9 illustrates the global stress distribution along the building height under the downburst wind profiles P1 ($z_{\bar{U}_{max}}$ = 30 m), P2 ($z_{\bar{U}_{max}}$ = 50 m) and P3 ($z_{\bar{U}_{max}}$ = 70 m). The higher stress concertation appears across the first ten storeys of the building for profiles P1 and P3, whereas the stress concentration under wind profile P2 intensifies in the neighbourhood of storeys 4 and 8 and at the base of column G1. This highlights once again that the position of $\bar{U}_{max}$ in a thunderstorm downburst strongly influences strength and ductility demands on buildings.

6 | EARTHQUAKE AND THUNDERSTORM DOWNBURST MULTI-HAZARD ANALYSIS

6.1 | Effect of multi-hazard events with varying height of $\bar{U}_{max}$

The base shear-roof drift relationship of the multi-hazard analysis is illustrated in Figure 10. By performing a pushover analysis, the frame reaches the following ductility levels, hence damage states: DL1, DL2, DL3, DL4, DL5 and DL6. For each damage state, a restart dynamic analysis is performed by subjecting the deformed frame to the three simulated downburst

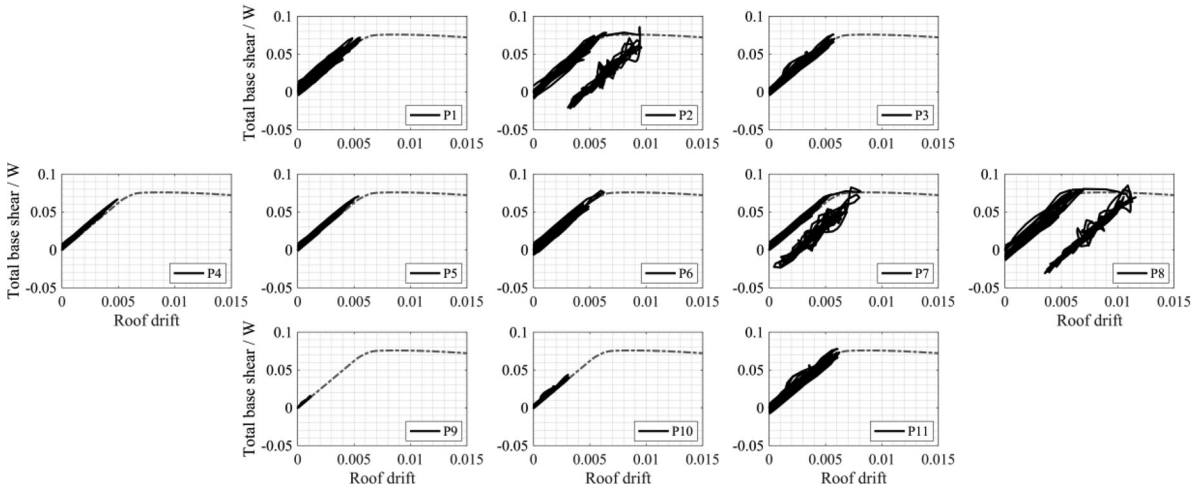

FIGURE 7 Comparison of the building frame responses under different downburst profiles (Grey dash line represents the pushover curves as shown in Figure 4).

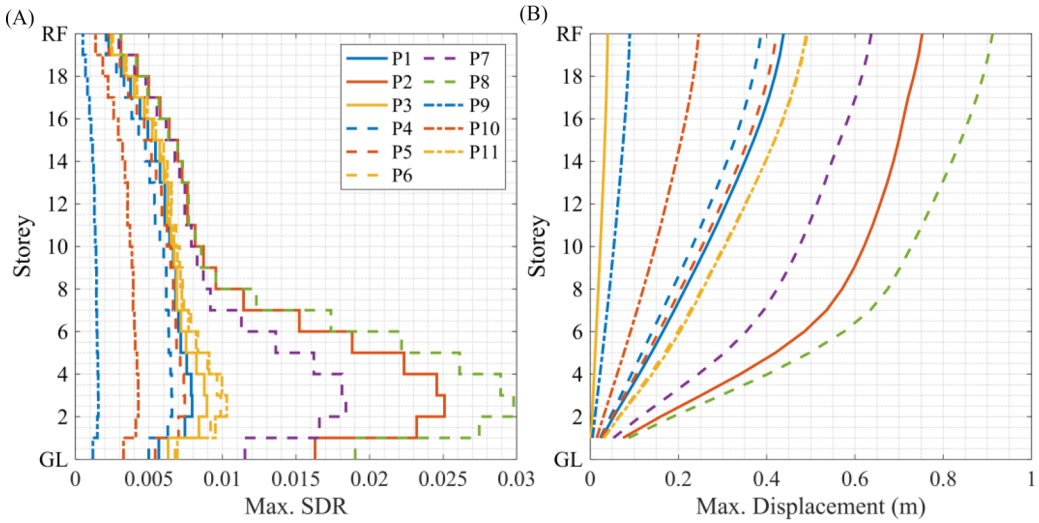

FIGURE 8 (A) Profile of the maximum SDRs and (B) Profile of the maximum displacements along the building height under the thunderstorm downbursts.

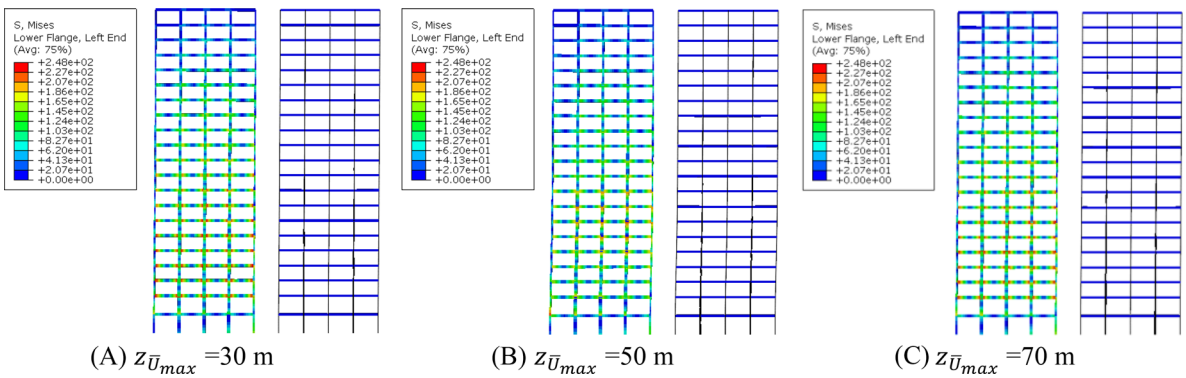

FIGURE 9 Global stress distribution at the time of maximum displacement under the downburst wind profile P1, P2 and P3.

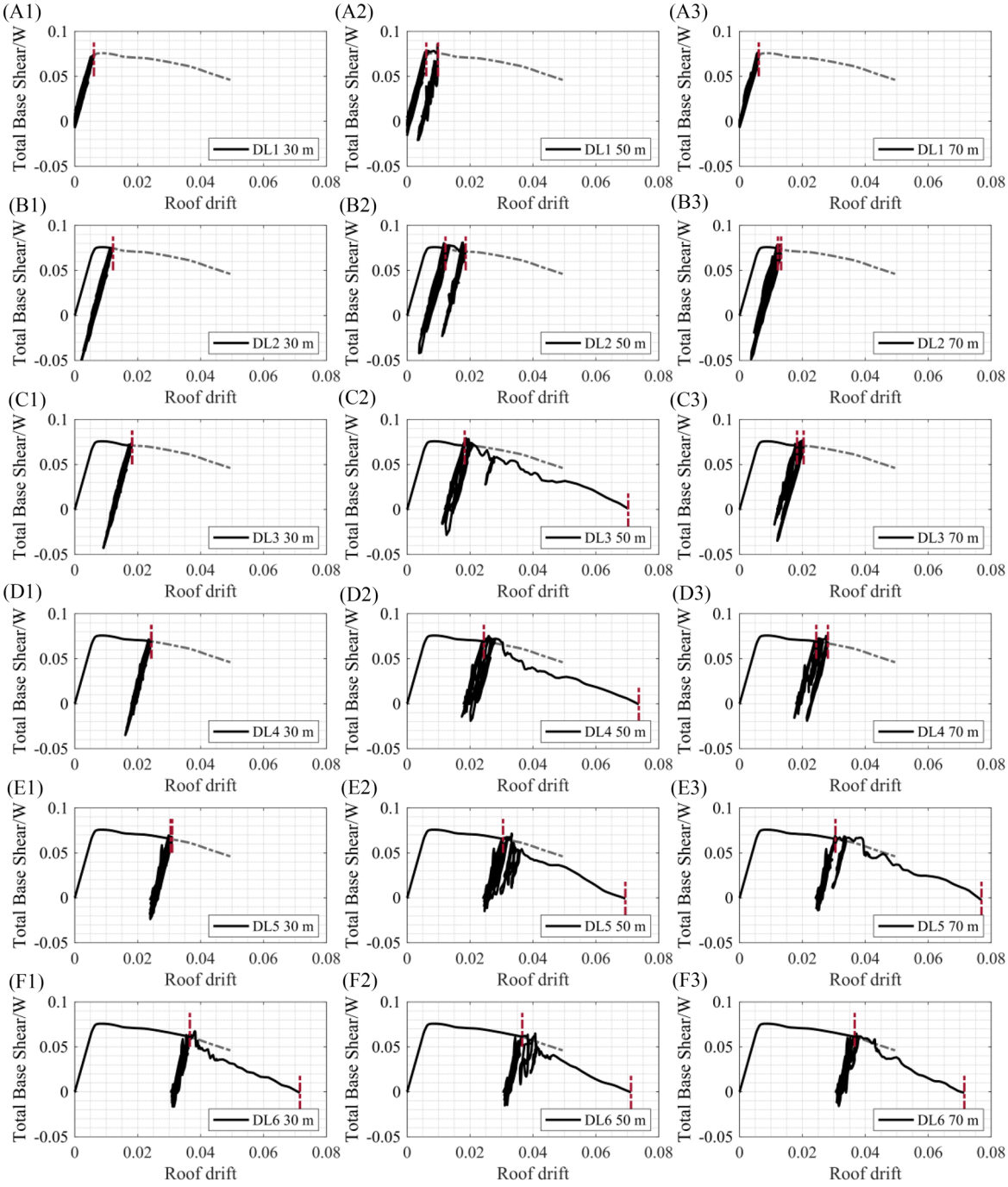

FIGURE 10 Comparison of the multi-hazard earthquake-thunderstorm response with varying $z_{\bar{U}_{max}}$, (A) DL1-Downburst; (B) DL2-Downburst; (C) DL3-Downburst; (D) DL4-Downburst; (E) DL5-Downburst; (F) DL6-Downburst (Grey dash line represents the pushover curves as shown in Figure 4; Red dash line represents the maximum displacement after the primary and secondary hazards separately).

wind profiles with varying height of $\bar{U}_{max}$ (i.e. 30, 50, 70m). The secondary ductility demands of the sequential analysis as obtained for each damage state are summarised in Table 2. In general, it can be seen from this table that as the primary target ductility level increases, the secondary ductility demands tend to increase (see red dash line in Figure 10).

Under the sequential analysis of the downburst wind profile P1, secondary ductility demands remained at the same level with those of the primary event indicating that the structure behaved almost elastically (Figure 10(A1) - (E1)). There might be some accumulation of damage for the structural elements, but this has not increased the roof displacement. A significant increase of secondary ductility demands which indicate global collapse is observed after reaching DL6 during the primary event (Figure 10(F1)). High-stress locations are observed between first and 10th storey for the primary damage

states DL1 and DL2 (see Figure 11(A1)–(B1)) and between first and 9th storey for the primary damage states DL3, and DL4 (see Figure 11(C1)–(D1)). For the primary damage states DL5 and DL6, a similar location of high stresses is observed between second and sixth storey (see Figure 11(E1)–(F1)).

Under the sequential analysis of the downburst wind profile P2, the structure responds inelastically and higher plastic deformations are observed than those during the wind profile P1. The maximum ductility is found to be 1.62 (0.78 m) and 3.05 (1.46 m) when the downburst event follows the primary damage states DL1 and DL2, respectively, which is a 62% and 52% increase of the initial ductility demand, respectively. High stresses are observed between the fourth and eighth storeys for primary damage state DL1 and between the first and ninth storeys of the building for primary damage state DL2 (see Figure 11(A2) and (B2)). The ductility demands increase significantly when the downburst event follows the primary damage states DL3, DL4, DL5 and DL6 resulting in four- and three-times higher ductility demands than those of the primary event, that is, 11.52, 12.07, 11.37 and 11.67, respectively (see Figure 10(C2)–(F2)). Excessive yielding areas are observed while steel beams have reached their maximum tensile strength. Under these ductility levels, a collapse mechanism has been formed that involves the second and sixth storey of the building, as shown in Figure 11(C2)–(F2).

Under the sequential analysis of the downburst wind profile P3, the ductility demands increase to 1.01, 2.17, 3.34 and 4.60 when the downburst event follows the primary damage states DL1, DL2, DL3 and DL4, which are 1%, 8.5%, 11.3% and 15% increase, respectively. The high-stress locations for profile 3 are like those for profile P1, but the building exhibited an overall collapse mechanism earlier. As shown in Figure 10(E3), global collapse is observed after reaching the primary damage state DL5.

The results of these three analysis profiles demonstrate that although the maximum velocity of the downburst occurs in profile P3, the downburst wind profile P2 imposes higher ductility demands leading the structure to global collapse. These results indicate that the height at which the maximum wind velocity occurs alongside with the shape of the vertical wind profile are two important parameters for consideration as they control the input energy and excessive plastic deformations of the structure.

6.2 | Effect of multi-hazard events with varying vertical profiles of I_u

This section discusses the ductility demands induced by thunderstorm downbursts with varying vertical profiles of turbulence intensities derived for terrain types 0, I, II, III and IV. The maximum velocity varies from 50 to 65 m/s for the different terrain type. The height of $\bar{U}_{max}$ for these wind events equals 50 m.

As shown in Figure 12 for the wind profile P4 and terrain type 0 (TT0), the secondary ductility demands induced by the downburst wind loads tend to increase with the primary target ductility level. The occurrence of the downburst has almost no effect when the building has experienced a primary damage state of DL1, DL2 and DL3, but has a notable impact on the overall ductility when the building has experienced a primary damage state of DL4, DL5 and DL6. The secondary ductility demands induced by subsequential secondary hazard in these damage states become 4.23 (DL4), 5.36 (DL5) and 7.18 (DL6), respectively (Table 2).

The results for the wind profile P5 and terrain type 1 (TT1) follow similar patterns to those reported for TT0 and wind profile P4. The secondary hazard event imposes ductility demands below a 1.08 magnification threshold for primary damage state DL1 - DL4 compared with those from the primary hazard event. In contrast, the accumulated secondary ductility demands of 11.84 and 11.96 nearly duplicate the primary ductility demands for primary damage state DL5 and DL6, respectively, since the building frame has collapsed, as shown in Figure 12.

The increase of ductility demand discussed above appears to have the same trend for TTII, TTIII, and TTIV under wind profiles P6-P8, but a more notable accumulation of damage alongside with increased roof displacements is observed. With the increase of the turbulence intensities under the same primary damage state, the accumulated secondary ductility demands are obviously increased, and the collapse of the building can happen even when the ductility levels of the primary damage state are lower. For instance, the ductility demands increase from 2.00 (0.96 m roof displacement) to 3.67 (1.76 m roof displacement) during the wind profiles of P4 to P8 (see Table 2) for the primary damage state DL2. The collapse of the building under wind profile P6 (TTII) happens at the primary damage state DL5, and the collapse of the building under wind profiles P7 (TTIII) and P8 (TTIV) occur at the primary damage states DL4 and DL3.

Therefore, when the slowly varying mean velocities and the simulated rapidly varying turbulent fluctuations are the same, downburst wind fields under varying turbulence intensities from different terrain types can influence the ductility demands of the damaged steel structures since higher velocity occurs with the increase in slowly varying standard deviation of the simulated velocity time histories.

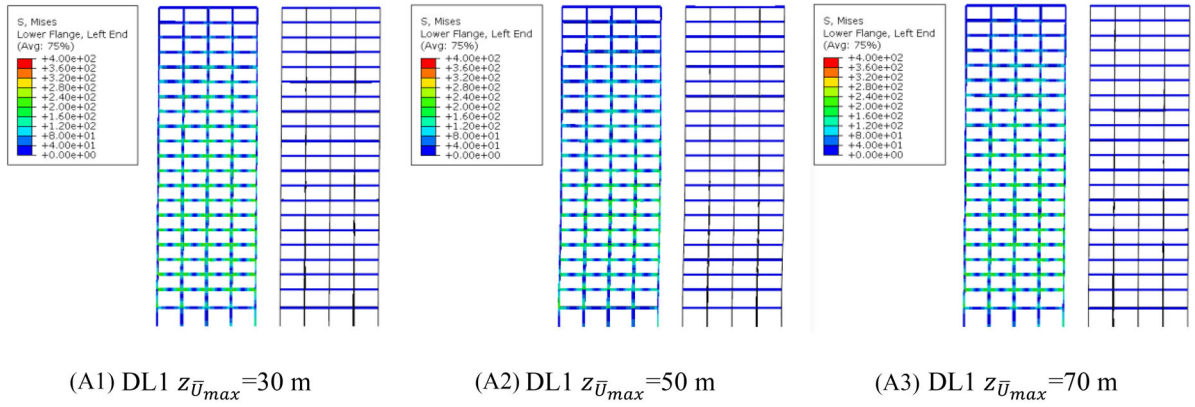

(A1) DL1 $z_{\bar{U}_{max}}$=30 m (A2) DL1 $z_{\bar{U}_{max}}$=50 m (A3) DL1 $z_{\bar{U}_{max}}$=70 m

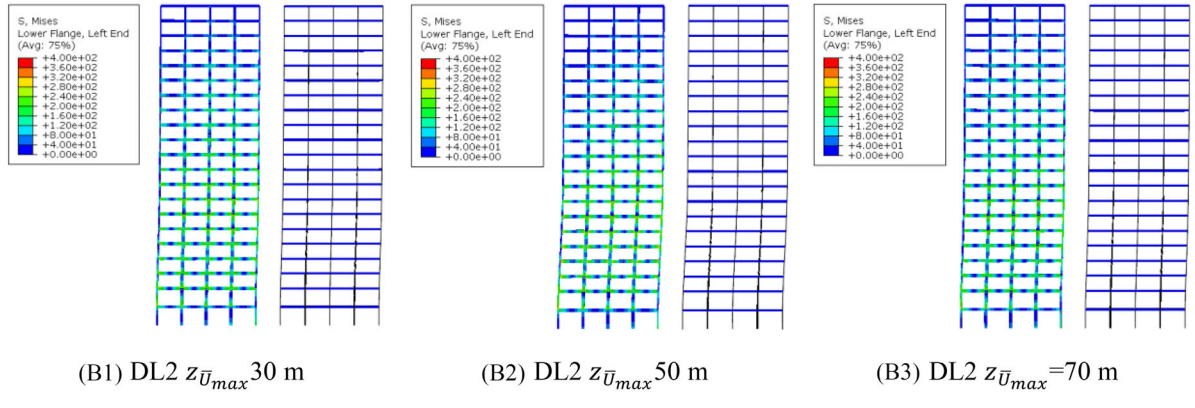

(B1) DL2 $z_{\bar{U}_{max}}$30 m (B2) DL2 $z_{\bar{U}_{max}}$50 m (B3) DL2 $z_{\bar{U}_{max}}$=70 m

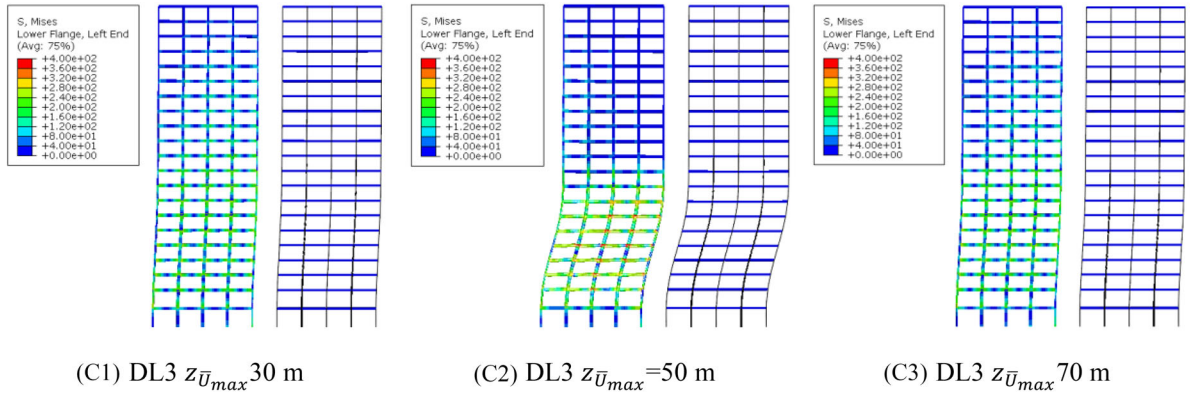

(C1) DL3 $z_{\bar{U}_{max}}$30 m (C2) DL3 $z_{\bar{U}_{max}}$=50 m (C3) DL3 $z_{\bar{U}_{max}}$70 m

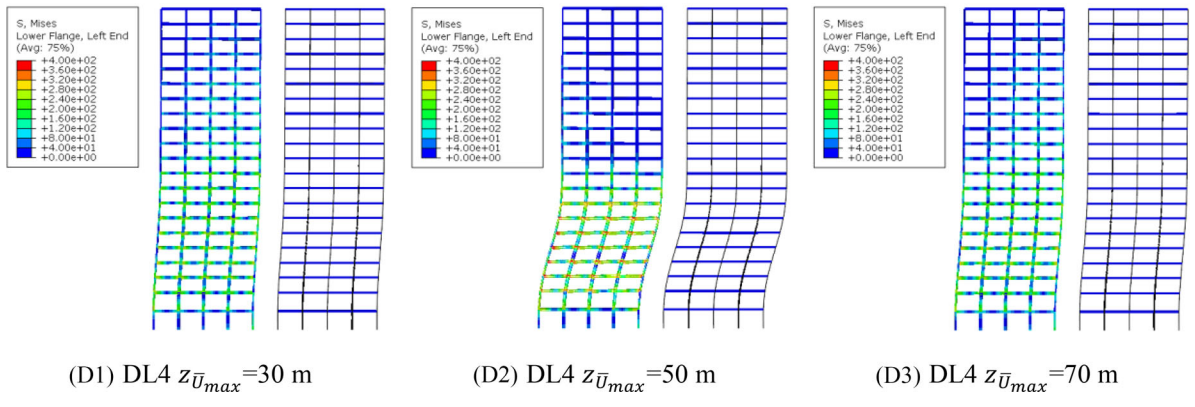

(D1) DL4 $z_{\bar{U}_{max}}$=30 m (D2) DL4 $z_{\bar{U}_{max}}$=50 m (D3) DL4 $z_{\bar{U}_{max}}$=70 m

FIGURE 11 Global stress distribution of the multi-hazard earthquake-thunderstorm response, (A) DL1-Downburst; (B) DL2-Downburst; (C) DL3-Downburst; (D) DL4-Downburst; (E) DL5-Downburst; (F) DL6-Downburst.

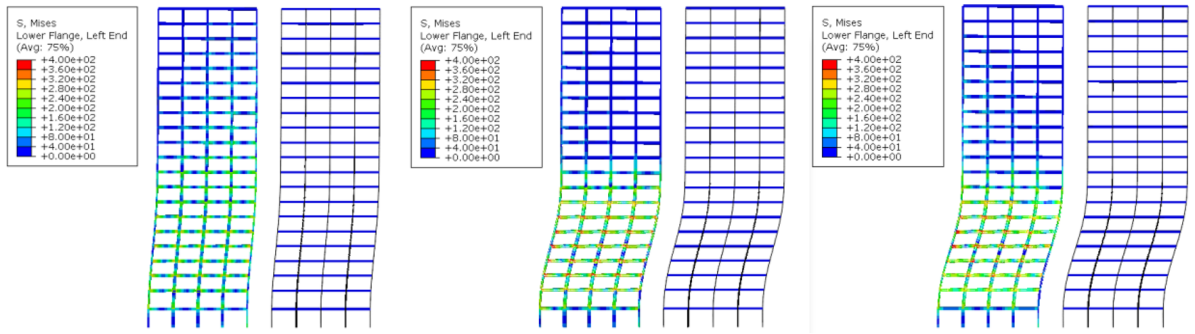

(E1) DL5 $z_{\bar{U}_{max}}$=30 m (E2) DL5 $z_{\bar{U}_{max}}$=50 m (E3) DL5 $z_{\bar{U}_{max}}$=70 m

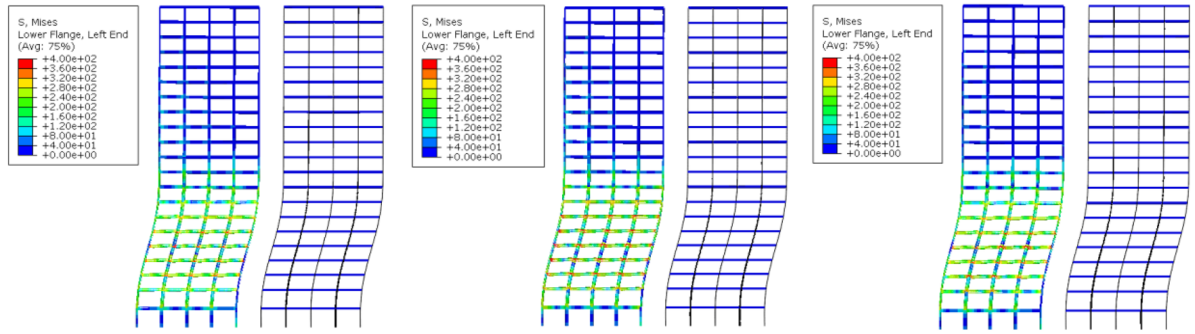

(F1) DL6 $z_{\bar{U}_{max}}$=30 m (F2) DL6 $z_{\bar{U}_{max}}$=50 m (F3) DL6 $z_{\bar{U}_{max}}$=70 m

FIGURE 11 Continued

6.3 | Effect of multi-hazard events with varying U_{max}

The multi-hazard analysis with stronger secondary thunderstorm downburst events, that is, higher maximum velocity, acting on the building frame illustrates a more obvious increase in ductility demand or a higher probability of building collapse. To gain a better understanding of the extent to which thunderstorm downburst events can influence damaged structures caused by primary hazard events, this section investigates the impact of downburst wind loads with varying maximum velocities. In this analysis, the height of $\bar{U}_{max}$ is 70 m and I_u comes from exposure B of terrain category in ASCE7,[16] while the selected maximum velocity levels are 30, 50 and 70 m/s.

The results show that accumulated secondary ductility demands of the building frame for all the primary damage state DL1-DL6 remain within the 1.04 magnification threshold when the maximum velocity reaches 30 and 50 m/s (see Table 2) and no global collapse happens, as shown in Figure 13(A1)–(F2). That threshold is exceeded for all primary ductility DL1-DL6 when the maximum velocity reaches 70 m/s. Notably, the accumulated secondary ductility demand of 13.11 recorded for DL5 is over two times of the ductility demands induced during the primary hazard event. Finally, the analyses in Figure 13 show the same collapsing mechanism observed during the previous parametric scenarios shown in Figures 10 and 12.

6.4 | Ductility demands and strength reduction

6.4.1 | Earthquake-wind ductility demands

Figure 14A plots the ductility demands induced by the earthquake loads (μ_1) against the accumulated earthquake-wind ductility demands (μ_2) as obtained after the application of the downburst wind profiles P1-P3. In Figure 14, four regions (S1-S4) are identified that qualitatively delimit the deformation state of the structure. The region S1 represents the elastic deformation stage, where $\mu_2 = \mu_1$ and lower than one; the region S2 represents the plastic deformation stage as

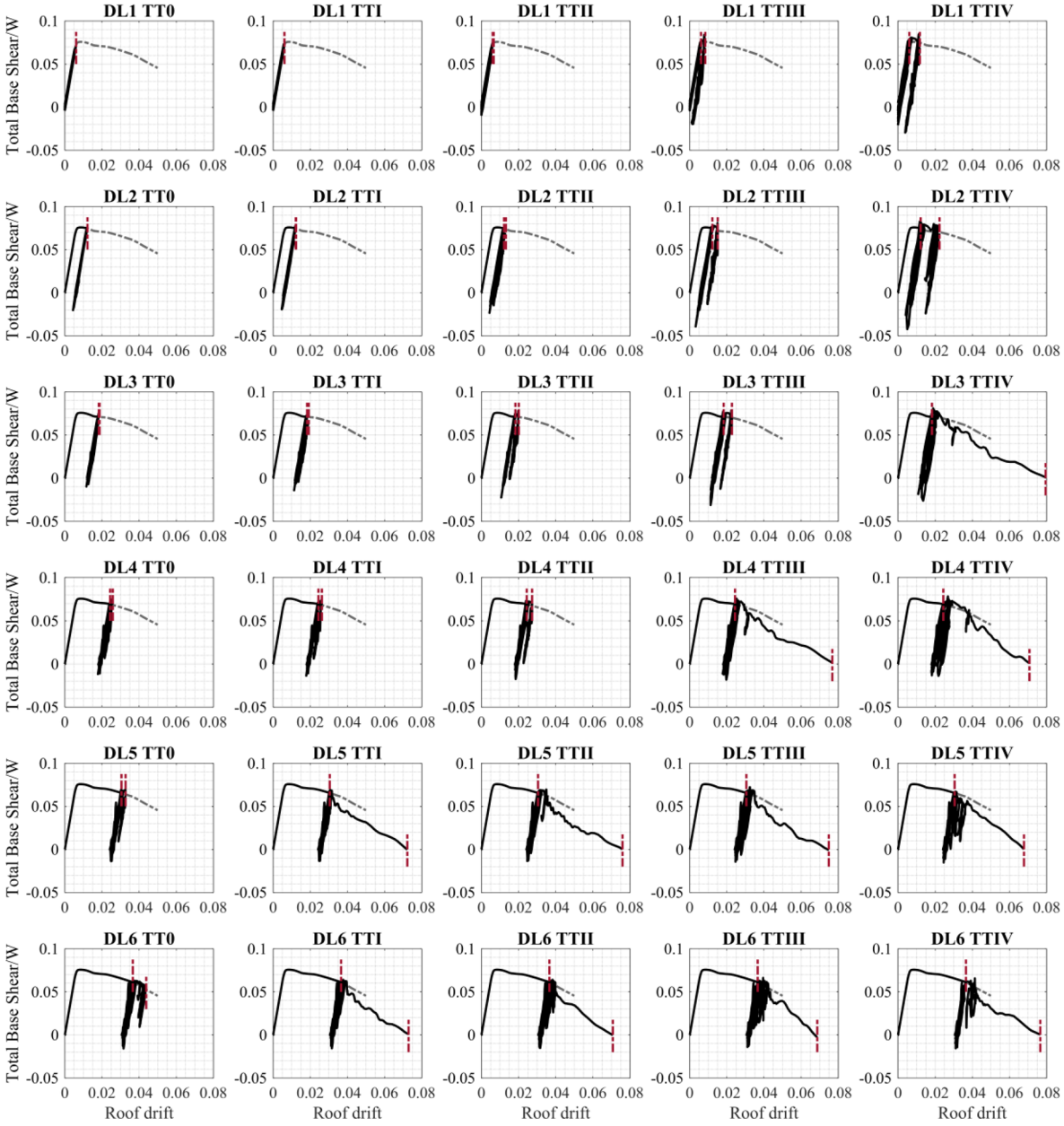

FIGURE 12 Comparison of the multi-hazard earthquake-thunderstorm response with varying vertical profiles of I_u from variable terrain types (0, I, II, III, IV), (Grey dash line represents the pushover curves as shown in Figure 4; Red dash line represents the maximum displacement after the primary and secondary hazards separately).

obtained for any targeted damage level, where $\mu_2 = \mu_1$ or $\mu_2 > \mu_1$ depending on the impact of the downburst profile to the earthquake-damaged buildings; the region S3 identifies pre-failure mechanisms of the structure (i.e. transition from stage S2 to stage S4), where always $\mu_2 > \mu_1$; and the region S4 refers to complete collapse of the structure (zero lateral forces). In Figure 14A, it can be observed that μ_2 suddenly progresses into stage S3 when $\mu_1 > 5$ for the thunderstorm scenario of $z_{\bar{U}_{max}} = 30$ m (wind profile P1), but no obvious increase of μ_2 is observed when the structure is subject to the same wind profile for $\mu_1 \leq 5$ (i.e. $\mu_2 \approx \mu_1$ in the region S2). When the $z_{\bar{U}_{max}}$ is 50 m (wind profile P2), $\mu_2 > \mu_1$ within the region S2, thus earthquake-wind ductility demands are higher than the earthquake-alone ductility demands (e.g. $\mu_2 = 3.05$ for $\mu_1 = 2$; this indicates a 53% increase of the ductility demands when downburst is considered). The structure is very likely to collapse after the application of the thunderstorm downburst if the earthquake-alone ductility demands are in the range of: $2 < \mu_1 < 3$. The earthquake-wind ductility demands for $z_{\bar{U}_{max}} = 70$ m (wind profile P3) are found to be in-between those obtained from the other two profiles. Ductility values μ_2 slightly increase within the

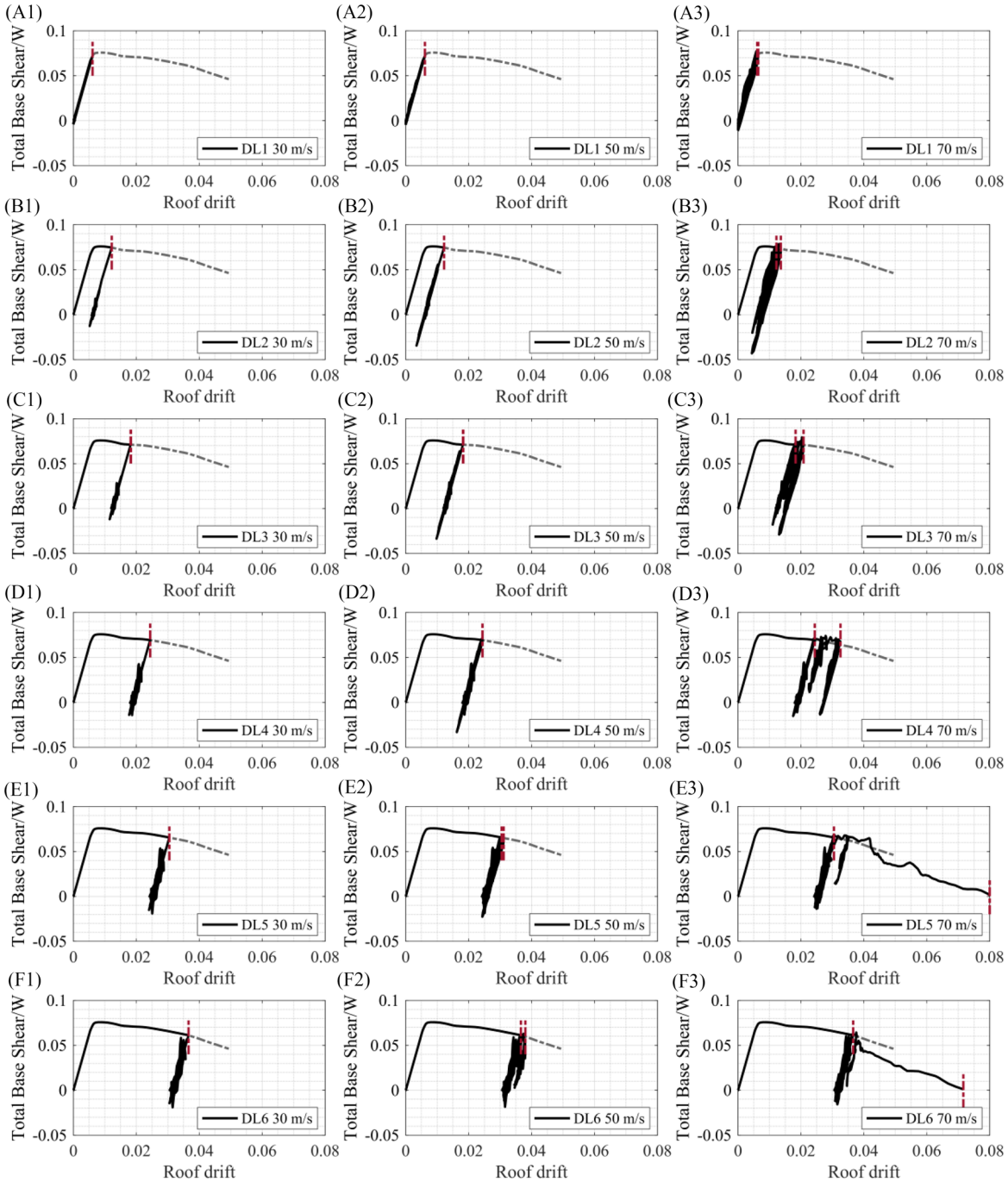

FIGURE 13 Comparison of the multi-hazard earthquake-thunderstorm response with varying U_{max} (Grey dash line represents the pushover curves as shown in Figure 4; Red dash line represents the maximum displacement after the primary and secondary hazards separately).

region S2 (e.g. $\mu_2 = 4.6$ for $\mu_1 = 4$; <15% increase), which indicates moderate damage accumulation by the thunderstorm downbursts.

Figure 14B summarises the analysis results with the same manner as in Figure 14A, but for wind profiles P4-P8, that is, turbulence intensity profiles associated to different ground roughness (terrain types). The results implied in curves $I_{u-TTIII}$ (profile P6) and I_{u-TTIV} (profile P7) report a high level of cumulative damage induced by the downburst wind events. For example, μ_2 is about 24% higher that μ_1 in the range S2, whereas collapse mechanisms would develop for higher levels of μ_1 (i.e. $\mu_1 > 2$) which is also highlighted in Table 2. In contrast, curve I_{u-TT0} (wind profile P4) does not suggest serious damage during the downburst, notwithstanding there is some increase of μ_2 (up to 6% of μ_1) when $\mu_1 = 6$. Profiles

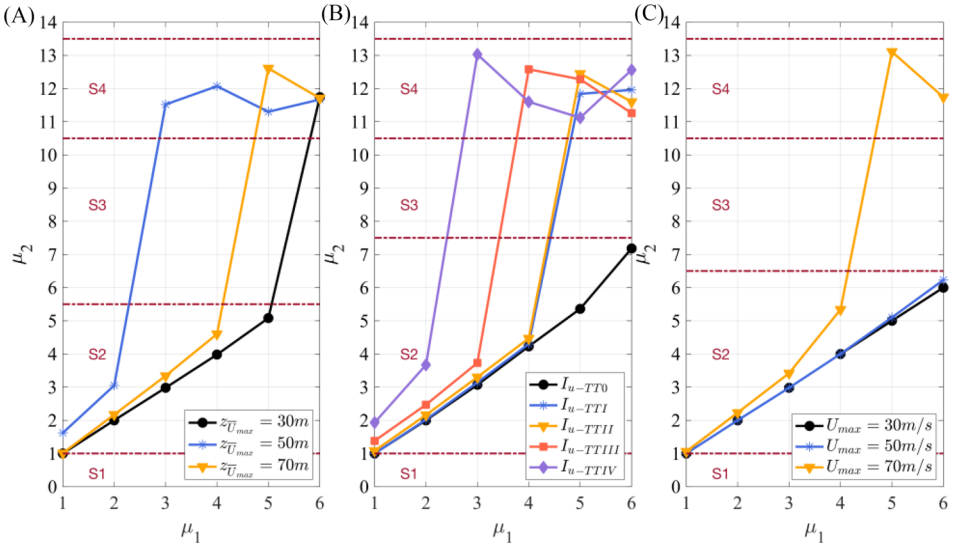

FIGURE 14 Ductility demands induced by the earthquake loads (μ_1) against the accumulated earthquake-wind ductility demands (μ_2) for eleven downburst wind fields, (A) Profile P1-P3; (B) Profile P4-P8; (C) Profile P9-P11.

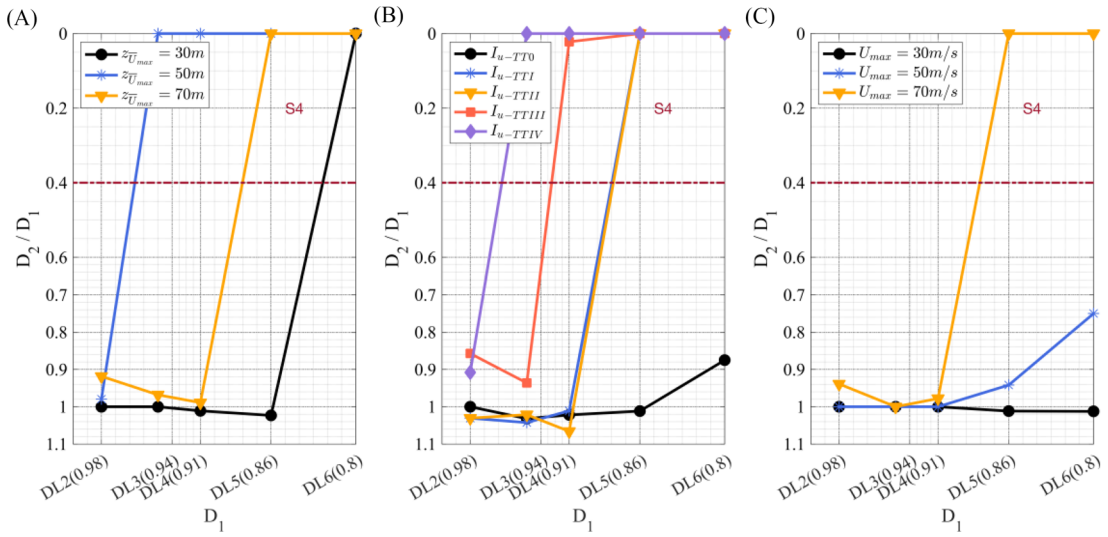

FIGURE 15 Accumulated deterioration of strength after the sequential earthquake-wind hazards considering, (A) Profile P1-P3; (B) Profile P4-P8; (C) Profile P9-P11.

I_{u-TTI} (profile P5) and I_{u-TTII} (profile P6) reveal moderate damage accumulation during the secondary hazard at low and medium initial ductility demands ($\mu_1 \leq 4$). For example, a relatively small increase of μ_2 (up to 12% of μ_1) in range S2 is observed. The same profile leads to significant increase of μ_2 for $\mu_1 = 5$ and $\mu_1 = 6$.

Figure 14C shows the results when changing the maximum horizontal wind speed during the secondary hazard. The critical scenarios appear when U_{max} equals 70 m/s (profile 11), as μ_2 are approximately 34% higher than μ_1 in the range of S2. Notably, plastic mechanisms could lead to collapse when μ_1 exceeds 5.

6.4.2 | Deterioration of strength

In Figure 4, it can be observed that the base shear the structure withstands after reaching a higher ductility level, decreases with respect to its yield strength. This process of deterioration is quantified in Figure 15 for each sequential hazard through

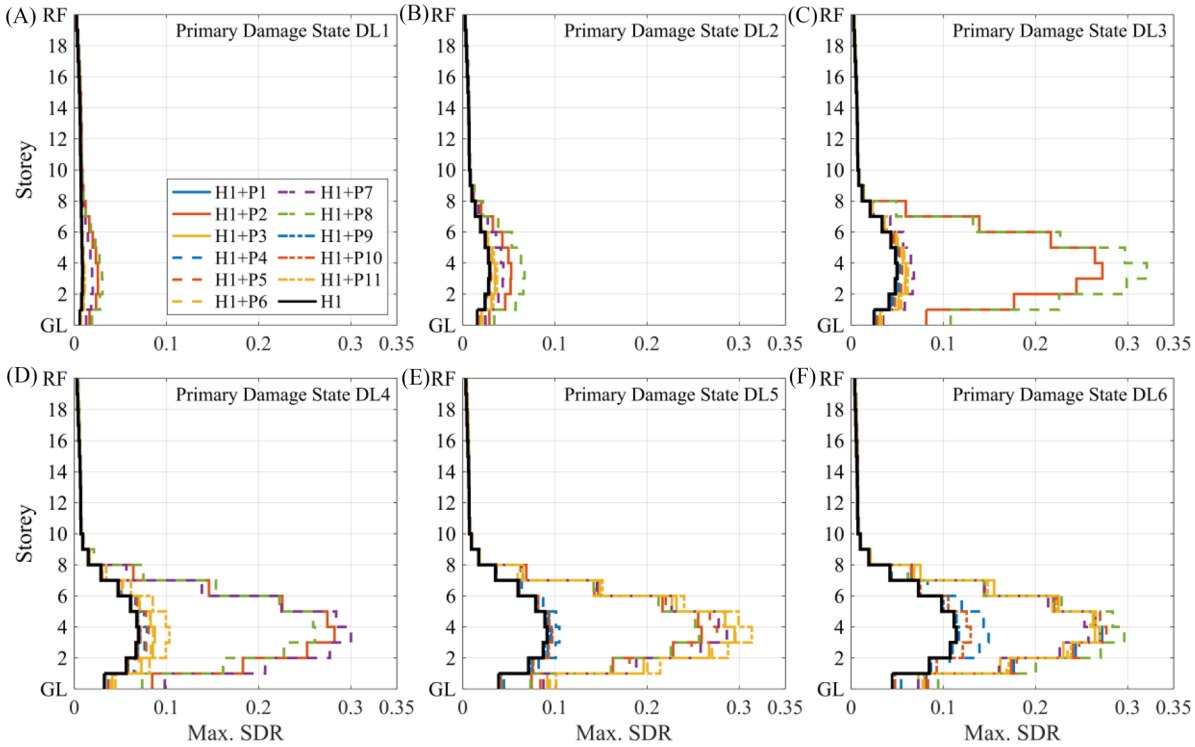

FIGURE 16 Maximum SDRs profile for (A) DL1-Downburst; (B) DL2-Downburst; (C) DL3-Downburst; (D) DL4-Downburst; (E) DL5-Downburst; (F) DL6-Downburst (H1 denotes the primary hazard alone).

the parameters D_1 and D_2. The rate of deterioration thus relates the base shear ordinate at the corresponding DL divided by the maximum base shear strength.

In Figure 15, all wind profiles drastically undermine building's integrity past the initial damage that induces DL6. This is also true for some lower ductility levels. For example, the deterioration induced by wind profiles P2 and P8 associated to DL3, DL4 and DL5, moves the building condition to region S4. In most cases, once the structure has reached DL5 and DL6, it rapidly moves to the collapse region under the effect of a downburst outflow.

Figures 16 and 17 illustrate the deterioration of strength from a different angle. These figures show the profile of the maximum SDRs and maximum displacements along the height of the structure, respectively. The incremental deterioration becomes evident when referring SDRs and displacements to effect of the primary hazard acting alone – that is labelled H1 in the plots. According to these metrics, the magnification of damage could triple after the secondary hazard takes place, particularly for high initial ductility levels. The rate of deterioration decreases as the initial ductility level approaches DL1, although in all cases, damage concentrates in the bottom third of the structure, where additional strength demands induced by thunderstorm downbursts accelerate the expansion of plastic material performance.

7 | CONCLUSION

The occurrence of extreme wind events, like thunderstorm downburst, within the lifetime of a structure may increase the design demands on structures that have been primarily designed against different type of loads. This study develops a multi-hazard analysis framework for evaluating the impact of secondary hazard events on strucutres that have previously been affected by primary hazardous events. More specifically, the present work investigates the effects of thunderstorm downbursts on earthquake-damaged 20-storey steel buildings giving an emphasis in assessing the revised accumulated earthquake-wind ductility demands. Based on the results of this study, the following conclusions can be drawn:

- The proposed multi-hazard analysis framework offers a robust implementation of earthquake pushover analysis and wind nonlinear time-history analysis within a novel restart analysis algorithm that allows a parametric study to be

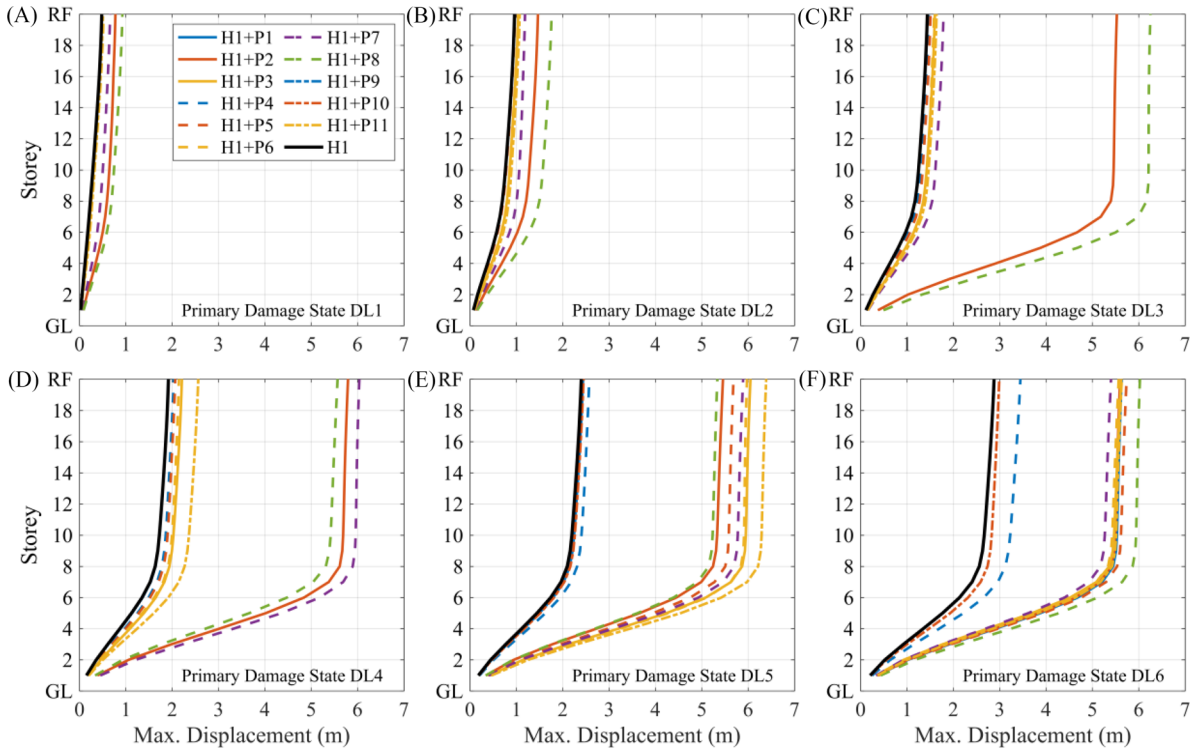

FIGURE 17 Maximum displacement profile for (A) DL1-Downburst; (B) DL2-Downburst; (C) DL3-Downburst; (D) DL4-Downburst; (E) DL5-Downburst; (F) DL6-Downburst (H1 denotes the primary hazard alone).

performed investigating various combinations of multi-hazard loads. This can provide effective guidance in the stage of structural design under multi-hazards or post-hazard assessment of structures identifying new serviceability limits, as well as reduce the risk of structural collapse under extreme secondary hazard events.

- The input energy induced by the subsequent downburst event may drive the structure from elasticity to plasticity, or reinforce the plastic deformation, thus exceeding the primary single-hazard ductility demands. The level of damage exhibited by the structure during the secondary wind event increases with the ductility demands generated by the primary earthquake event.
- There are scenarios in which the sequence of hazards does not induce collapse, however, at low inelastic levels ductility demands may increase nearly up to 100% due to the secondary hazard (e.g. from earthquake-induced ductility demands of one to a revised multi-hazard earthquake-wind ductility of 1.93), which severely undermines the serviceability of the building. On the other hand, at high inelastic levels it was observed that total ductility demands may double or quadruple under subsequent damaging thunderstorms resulting in a sudden global collapse of the structure.
- The proposed analysis framework can produce superior numerical results as well as accurately identify the overall plastic deformation mechanism of the structure until global collapse. Collapse that involves the first to eighth storey of the building is likely to occur under the multi-hazard earthquake/thunderstorm analysis when the primary event has induced a ductility demand range from 3 to 5. This was further illustrated when analysing the profile of SDRs and maximum displacements along the height of the structure.
- The results of this study also highlight the influence of the position of the peak horizontal velocity which also defines the shape of the vertical wind profile. The configuration of the wind field determines the rate of energy imparted by wind and influences the region of the building that first undergoes global plastic collapse mechanisms. The effects observed for the simulated wind profile P2 (U_{max} = 63 m/s), where the height of the maximum slowly varying mean velocity is 50 m, identify a critical load configuration (i.e. the resultant of the system of forces exerted by the wind is located in the transition from the middle to the top third of the building).
- Terrain conditions appears to be a critical parameter. Severe global plastic deformation mechanisms were observed in the building when the downburst did follow earthquake-induced ductility demands more than 2.0 for terrain types II, III and IV. Even though some of the adopted scenarios do not necessarily induce global collapse, the occurrence of a thunderstorm downburst can increase ductility demands after the earthquake up to 85% at the intermediate inelastic

levels for terrain type IV (e.g. from earthquake-induced ductility demands of 2.0 to a revised multi-hazard earthquake-wind ductility of 3.70) which may severely undermine the remnant capacity of the building.

ACKNOWLEDGEMENTS

The authors are thankfull to Miss Pelagia Kastiza, PhD student of University of Birmingham, for her contribution in the development of the building finite element model.

DATA AVAILABILITY STATEMENT

The data that support the findings of this study are available from the corresponding author upon reasonable request.

ORCID

Jing Song https://orcid.org/0000-0003-3269-1865
Konstantinos Skalomenos https://orcid.org/0000-0002-0734-3992

Note

[1]SDR defined as the storey drift divided by the height of the storey

REFERENCES

1. Li Y, Song R, Van De Lindt JW. Collapse fragility of steel structures subjected to earthquake mainshock-aftershock sequences. *J Struct Eng*. 2014;140(12):04014095.
2. Rossetto T, De la Barra C, Petrone C, De la Llera JC, Vásquez G J, Baiguera M. Comparative assessment of nonlinear static and dynamic methods for analysing building response under sequential earthquake and tsunami. *Earthq Eng Struct Dyn*. 2019;48(8):867-887.
3. Brooks HE. Severe thunderstorms and climate change. *Atmos Res*. 2013;123:129-138.
4. Rädler AT, Groenemeijer PH, Faust E, Sausen R, Púčik T. Frequency of severe thunderstorms across Europe expected to increase in the 21st century due to rising instability. *npj Clim Atmos Sci*. 2019;2(1):1-5.
5. Fujita TT. *The downburst: Microburst and Macroburst*. The University of Chicago; 1985
6. Lombardo FT, Smith DA, Schroeder JL, Mehta KC. Thunderstorm characteristics of importance to wind engineering. *J Wind Eng Ind Aerodyn*. 2014;125:121-132.
7. Fujita TT. Downbursts: meteorological features and wind field characteristics. *J Wind Eng Ind Aerodyn*. 1990;36:75-86.
8. Caracoglia L. Unified stochastic dynamic and damage cost model for the structural analysis of tall buildings in thunderstorm-like winds. *ASCE*. 2018;4(4):04018043.
9. Solari G, De Gaetano P. Dynamic response of structures to thunderstorm outflows: response spectrum technique vs time-domain analysis. *Eng Struct*. 2018;176:188-207.
10. Kareem A, Hu L, Guo Y, Kwon D-K. Generalized wind loading chain: Time-frequency modeling framework for nonstationary wind effects on structures. *J Struct Eng*. 2019;145(10):04019092.
11. Ciano M, Gioffrè M, Gusella V, Grigoriu MD. Non-stationary dynamic structural response to thunderstorm outflows. *Probab Eng Mech*. 2020;62:103103.
12. Song J, Martinez-Vazquez P, Skalomenos KA. A framework on the dynamic response of tall structures to non-stationary wind using design spectrum. *8th ECCOMAS Thematic Conference on Computational Methods in Structural Dynamics and Earthquake Engineering*, Athens, Greece, 2021.
13. Krishnan S. Case studies of damage to tall steel moment-frame buildings in southern California during large San Andreas earthquakes. *Bull Seismol Soc Am*. 2006;96(4A):1523-1537.
14. Loredo-Souza AM, Lima EG, Vallis MB, Rocha MM, Wittwer AR, Oliveira MGK. Downburst related damages in Brazilian buildings: Are they avoidable? *J Wind Eng Ind Aerodyn*. 2019;185:33-40.
15. Tilloy A, Malamud BD, Winter H, Joly-Laugel A. A review of quantification methodologies for multi-hazard interrelationships. *Earth Sci Rev*. 2019;196:102881.
16. ASCE7. *Minimum Design Loads for Buildings and Other Structures (ASCE/SEI 7–10)*. American Society of Civil Engineers; 2013
17. Eurocode, 1: Actions on structures–Part 1.4: General actions–wind actions. *Brussels: The European Standard EN*, 2010.
18. Code P. *Eurocode 8: Design of structures for earthquake resistance-part 1: general rules, seismic actions and rules for buildings*. Brussels: European Committee for Standardization; 2005.
19. Duthinh D, Simiu E. Safety of structures in strong winds and earthquakes: multihazard considerations. *J Struct Eng*. 2010;136(3):330-333.
20. Duthinh D, Potra F. Probabilistic and Optimization Considerations in Multihazard Engineering, in *Vulnerability, Uncertainty, and Risk: Analysis, Modeling, and Management*. 2011:501-509.
21. Aly AM, Abburu S. On the design of high-rise buildings for multihazard: fundamental differences between wind and earthquake demand. *Shock Vibration*. 2015;2015:1-22.
22. Thilakarathna SN, Anwar N, Norachan P, Naja FA. The effect of wind loads on the seismic performance of tall buildings. *Athens J Technol Eng*. 2018;5(3):251-276.

23. Kim T, Han SW, Cho SI. Effect of wind loads on collapse performance and seismic loss for steel ordinary moment frames. *Appl Sciences*. 2022;12(4):2011.
24. Martinez-Vazquez P. Strength reduction factors for wind and earthquake effects. *Proc Inst Civ Eng: Struct Build*. 2017;170(10):735-750.
25. Martinez-Vazquez P, Gkantou M, Baniotopoulos C. Strength and ductility demands on wind turbine towers due to earthquake and wind load. *Proc Inst Civ Eng: Struct Build*. 2019;172(8):556-563.
26. Martin J, Alipour A, Sarkar P. Fragility surfaces for multi-hazard analysis of suspension bridges under earthquakes and microbursts. *Eng Struct*. 2019;197:109169.
27. Roy T, Saito T, Matsagar V. Multihazard framework for investigating high-rise base-isolated buildings under earthquakes and long-duration winds. *Earthq Eng Struct Dyn.* 2021;50(5):1334-1357.
28. Kwag S, Gupta A, Baugh J, Kim H-S. Significance of multi-hazard risk in design of buildings under earthquake and wind loads. *Eng Struct*. 2021;243:112623.
29. Elias S, Rupakhety R, Olafsson S. Analysis of a benchmark building installed with tuned mass dampers under wind and earthquake loads. *Shock Vibrat*. 2019;2019:1-13.
30. Taha A. Vibration control of a tall benchmark building under wind and earthquake excitation. *Pract Period Struct Des Constr*. 2021;26(2):04021005.
31. Bracci JM, Kunnath SK, Reinhorn AM. Seismic performance and retrofit evaluation of reinforced concrete structures. *J Struct Eng*. 1997;123(1):3-10.
32. Abbasnia R, Davoudi AT, Maddah MM. An adaptive pushover procedure based on effective modal mass combination rule. *Eng Struct*. 2013;52:654-666.
33. Abaqus User's Manual, 2021. Providence, Rohde Island, USA: Dassault Systemes. Simulia Corporation ABAQUS version 2021.
34. Chopra AK, Goel RK. A modal pushover analysis procedure for estimating seismic demands for buildings. *Earthq Eng Struct Dyn*. 2002;31(3):561-582.
35. MathWorks, Inc. MATLAB R2022b. Natick, MA: MathWorks, Inc., 2022.
36. Skalomenos KA, Papazafeiropoulos G. A computational method for performing nonlinear adaptive pushover analysis of structures through ABAQUS simulation. *Proceedings of 7th COMPDYN*. Heraklion, Crete, Greece; 2019.
37. Panyakapo P. Cyclic pushover analysis procedure to estimate seismic demands for buildings. *Eng Struct*. 2014;66:10-23.
38. Skalomenos KA, Kurata M, Nakashima M. On-line hybrid test method for evaluating the performance of structural details to failure. *Earthq Eng Struct Dyn*. 2018;47(3):555-572.
39. Skalomenos KA, Nakashima M, Kurata M. Seismic capacity quantification of gusset-plate connections to fracture for ductility-based design. *J Struct Eng*. 2018;144(10):04018195.
40. Hilber HM, Hughes TJ, Taylor RL. Improved numerical dissipation for time integration algorithms in structural dynamics. *Earthq Eng Struct Dyn*. 1977;5(3):283-292.
41. Code UB. International conference of building officials (ICBO). Whittier, CA, 1994.
42. Hall JF. On the descending branch of the pushover curve for multistory buildings. *Earthq Eng Struct Dyn*. 2017;47(3):772-783.
43. Castiglioni C, et al. A Procedure for the Assessment of the Behaviour Factor for Steel MRF Systems Based on Pushover Analysis. *COMPDYN 2017*. 2017.
44. Chen L, Letchford C, A deterministic–stochastic hybrid model of downbursts and its impact on a cantilevered structure. *Eng Struct*. 2004;26(5):619-629.
45. Priestley MB. Evolutionary spectra and non-stationary processes. *J R Stat Soc Series B Stat Methodol*. 1965;27(2):204-229.
46. Deodatis G. Simulation of ergodic multivariate stochastic processes. *J Eng Mech*. 1996;122(8):778-787.
47. Solari G, Burlando M, De Gaetano P, Repetto MP. Characteristics of thunderstorms relevant to the wind loading of structures. *Wind Struct*. 2015;20(6):763.
48. Wood GS, Kwok KCS, Motteram NA, Fletcher DF. Physical and numerical modelling of thunderstorm downbursts. *J Wind Eng Ind Aerodyn*. 2001;89(6):535-552.
49. Holmes JD, Oliver S. An empirical model of a downburst. *Eng Struct*. 2000;22(9):1167-1172.
50. Solari G, De Gaetano P, Repetto MP. Wind loading and response of structures in mixed climates. *Proceedings of the Eight Asia Pacific Conference on Wind Engineering*. 2013.
51. Melbourne W. Comparison of measurements on the CAARC standard tall building model in simulated model wind flows. *J Wind Eng Ind Aerodyn*. 1980;6(1-2):73-88.

How to cite this article: Song J, Skalomenos K, Martinez-Vazquez P. A multi-hazard analysis framework for earthquake-damaged tall buildings subject to thunderstorm downbursts. *Earthquake Engng Struct Dyn*. 2023;1-23. https://doi.org/10.1002/eqe.3825